Winter 12-15-2019

Instrumentation for Dynamic Nuclear Polarization and Application of Electron Decoupling for Electron Relaxation Measurement

Nicholas Howard Alaniva
Washington University in St. Louis

WASHINGTON UNIVERSITY IN ST. LOUIS

Division of Chemistry

Dissertation Examination Committee:
Sophia E. Hayes, Chair
Alexander B. Barnes
Dewey Holten
Richard Mabbs
Cornelius von Morze

Instrumentation for Dynamic Nuclear Polarization and Application of Electron Decoupling for Electron Relaxation Measurement

by

Nicholas Howard Alaniva

A dissertation presented to
The Graduate School
of Washington University in
partial fulfillment of the
requirements for the degree
of Doctor of Philosophy

December 2019
St. Louis, Missouri

Table of Contents

List of Figures

List of Tables

Acknowledgments

I want to first thank my family: My mother and father for providing nothing but love and encouragement, and my sister for filling my life with laughter. They are the reason I am where I am, what I am, who I am, and why I believe that I can be what I want to be.

I want to thank the members of the Barnes Lab for making every day an adventure worth experiencing. I would like to specifically thank Dr. Erika Sesti, Dr. Edward Saliba, and Patrick Judge for the many months of conversation and camaraderie.

I would like to thank Jim Linders, without whom none of the instrumentation would have been possible.

I would like to thank all my friends outside the lab, those in St. Louis and abroad, for filling my time with so many memories.

Specifically, I would like to mention Emily Warner, alongside whom I have grown, from whom I have received support, and with whom I have experienced so many moments in life.

I would like to thank Lane Lohr, (Coach) Stiles, and Coach Reiter, under whose collective guidance I have grown as a member of a team. I specifically thank Lane Lohr for the unreal level of support, the invaluable lessons in persistence, and the countless memories that make me smile.

I would like to thank my Thesis Committee: Dr. Sophia Hayes, Dr. Richard Mabbs, and Dr. Alexander Barnes. Their time and input regarding my thesis and the trajectory of my work has been invaluable.

I would like to, again, thank Dr. Alexander Barnes. Dr. Barnes has facilitated my growth as a scientist and has supported me throughout my time as a graduate student.

Nicholas Alaniva

Washington University in St. Louis

December 2019

Dedicated to my parents and my sister.

ABSTRACT OF THE DISSERTATION

Instrumentation for Dynamic Nuclear Polarization

and Application of Electron Decoupling for Electron Relaxation Measurement

by

Nicholas Howard Alaniva

Doctor of Philosophy in Chemistry

Washington University in St. Louis, 2019

Professor Sophia E. Hayes, Chair

Dynamic nuclear polarization nuclear magnetic resonance (DNP NMR) exploits internal electron spin and nuclear spin interactions to increase sensitivity and uncover valuable information regarding structure and dynamics of a system. To manipulate these interactions, instrumentation is developed to combine high-power microwave and radiofrequency irradiation with the ability to spin samples at the magic angle (MAS) at temperatures from 90 K to 4.2 K. Electron decoupling uses frequency-modulated microwaves to mitigate the electron-nuclear dipolar interaction, improving signal intensity and resolution in DNP NMR experiments. Electron decoupling is combined with short DNP periods to encode electron spin information in polarized nuclear signal. The application of electron decoupling is expanded to a system of dilute ^{14}N-endohedral C_{60}.

Chapter 1: Introduction

1.1 Nuclear Magnetic Resonance

Nuclear Magnetic Resonance (NMR) is a spectroscopic technique that is impressive in the breadth of information it can provide on complex systems, and the detail and accuracy to which it can define a system's dynamics and structure [1-3]. This form of spectroscopy relies on the interaction of nuclear spins with internal and external components. The nuclear spins' interactions with an external magnetic field and applied radiofrequency (RF) irradiation generates the detectable signal and allows for manipulation of the spins, respectively. The interactions of the nuclear spins with internal components provides the valuable information regarding structure and dynamics; and the interaction of nuclear spins with unpaired electron spins can be exploited to enhance sensitivity. These interactions comprise the total NMR Hamiltonian, and the development of instrumentation and methods presented herein are inspired by the drive to control and exploit certain interactions.

Most of the spins discussed here are spin-½, meaning that, when subjected to an external magnetic field two distinct energy levels emerge. The separation of these levels is proportional to the strength of the external magnetic field and the gyromagnetic ratio (an inherent property of a spin; the ratio of a particle's magnetic moment to its angular momentum). The population of these two levels can be described by Boltzmann statistics, giving the following equation as the description of the polarization of the system:

$$P = tanh\left(\frac{\gamma \hbar B_0}{2Tk_B}\right)$$

Where P is the polarization, γ is the gyromagnetic ratio, $\hbar$ is the reduced Planck constant, B_0 is the external magnetic field, T is the temperature, and k_B is the Boltzmann constant. From this equation it is seen that increasing the gyromagnetic ratio and the external magnetic field, and decreasing the temperature results in a higher degree of polarization. The value γB_0 is called the Larmor frequency (also referred to as ω_0); in a classical point-of-view, the Larmor frequency describes the rate of precession of a spin's magnetic moment about the external magnetic field vector. To achieve resonance and manipulate spins, electromagnetic radiation at/near a spin's Larmor frequency is required. Here, nuclear spins with Larmor frequencies from 30 MHz – 300 MHz are controlled with RF irradiation, and electron spins with Larmor frequencies ~ 198 GHz are manipulated with microwave irradiation.

The crux of NMR is inherently weak signal, relative to noise. This low level of signal is due to the fact that the separation of the energy levels is not large, relative to the thermal energy present. To overcome this poor signal, methods like cross-polarization (CP) and dynamic nuclear polarization (DNP) NMR can be employed. CP and DNP NMR are two techniques that exploit the relatively high gyromagnetic ratio of ^{1}H spins (usually) and electron spins, respectively, to transfer the polarization of the more-polarized spins to the observed spins with smaller gyromagnetic ratios (^{13}C, ^{15}N), thus improving the signal-to-noise of the experiment [4].

CP and DNP require some external control/influence over the internal spin system. In the case of CP, and all other experiments that manipulate nuclear spins, RF irradiation of sufficient strength is required to facilitate polarization transfer from high-γ nuclei to low-γ nuclei. For DNP NMR, both RF and microwave irradiation are required. Current methods for DNP, which utilize continuous-wave microwave irradiation, mostly require cold (< 120 K) temperatures to be effective. This restriction is based on the need for slower longitudinal relaxation of the polarizing

electron spins. Thus, cryogenic temperatures are lucrative for more than just the improved Boltzmann polarization of the nuclear spins.

1.2 Solid-state Nuclear Magnetic Resonance

At cryogenic temperatures, samples that may have been a solution will be frozen. These samples, and solid samples in general, suffer an additional loss in both signal intensity and resolution due to the fact that fast molecular motion, like tumbling, is not present to the same degree that it is in liquid NMR. In liquids this motion averages out many internal anisotropic interactions, but in solids these interactions are present and serve to broaden the signal. However, resolution can be recovered by mitigating these interactions. Magic-angle spinning (MAS) at high enough frequency can average out anisotropic interactions that contain a certain angle-dependence. This dependency is described by the term, $(1 - 3\cos^2\theta)$. In MAS, the sample rotor is spun mechanically spun about an axis that is set at the "magic angle" of 54.7˚ with respect to the external magnetic field [4, 5]. Another way to mitigate these internal interactions is through decoupling. It is common practice to conduct nuclear spin decoupling with RF irradiation. With the frequency-agile microwave source described here, it is also possible to decouple paramagnetic electron spins from the observed nuclear spins.

1.2.1 Dynamic Nuclear Polarization

DNP, as mentioned above, is a process that utilizes the relatively large level of polarization present in electron spins to achieve greater nuclear signal. This process is facilitated by microwave irradiation whose frequency depends on the specific DNP mechanism, which depends on the characteristics of the polarizing agent, the source of the electron spin, itself. In this dissertation, the polarizing agents used employ one of two DNP mechanisms: the solid effect and the cross effect. Here, a "narrow-line radical" is used for solid effect and a "broad-line

radical" is used for the cross effect. These different mechanisms utilize microwave irradiation of different frequencies to facilitate the transfer of polarization from the radical electron to the nuclear spin. The values of these "matching conditions" depend on the electron paramagnetic resonance (EPR) frequency (referred to as ω_e) of the unpaired electron species.

DNP via the solid effect requires microwave irradiation equal to $\omega_e \pm \omega_0$ (nuclear Larmor frequency) [6,7]. A depiction of the solid effect mechanism is presented in **Figure 1.1**. Note, the assignment of the terms "double quantum" and "zero quantum" to the mechanism is dependent on the "direction" of the nuclear and electron spins relative to one another; this is determined by the sign of the gyromagnetic ratio. The different mechanisms will determine whether the polarization is "positive" (in-phase with the original nuclear signal) or "negative" (opposite phase of the original nuclear signal). **Figure 1.1** shows a qualitative depiction of the electron polarization resulting from microwaves that satisfy the zero quantum condition. In this scenario, the microwave irradiation connects the energy levels, creating a temporary degeneracy, thus the populations of those two levels become equal. In this process, the electron spin goes from spin-up to spin-down, and the nuclear spin from spin-down to spin-up (a net "zero quantum" effect). Ideally, the polarization of the nuclear spin levels will perfectly follow that of the electron levels. However, factors such as electron spin relaxation and the strength of the dipolar-hyperfine electron-nuclear interaction lead to less-than-optimal polarization transfer.

The solid effect condition is $\omega_e \pm \omega_0$, and thus, the radicals used here that employ the solid effect have EPR linewidths that are less than ω_0. The organic monoradical trityl that is featured here has an EPR linewidth of about 50 MHz when trityl is present at 40 mM. Another narrow-line polarizing agent described in this dissertation is the unpaired electron in an ^{14}N trapped within a C_{60} fullerene.

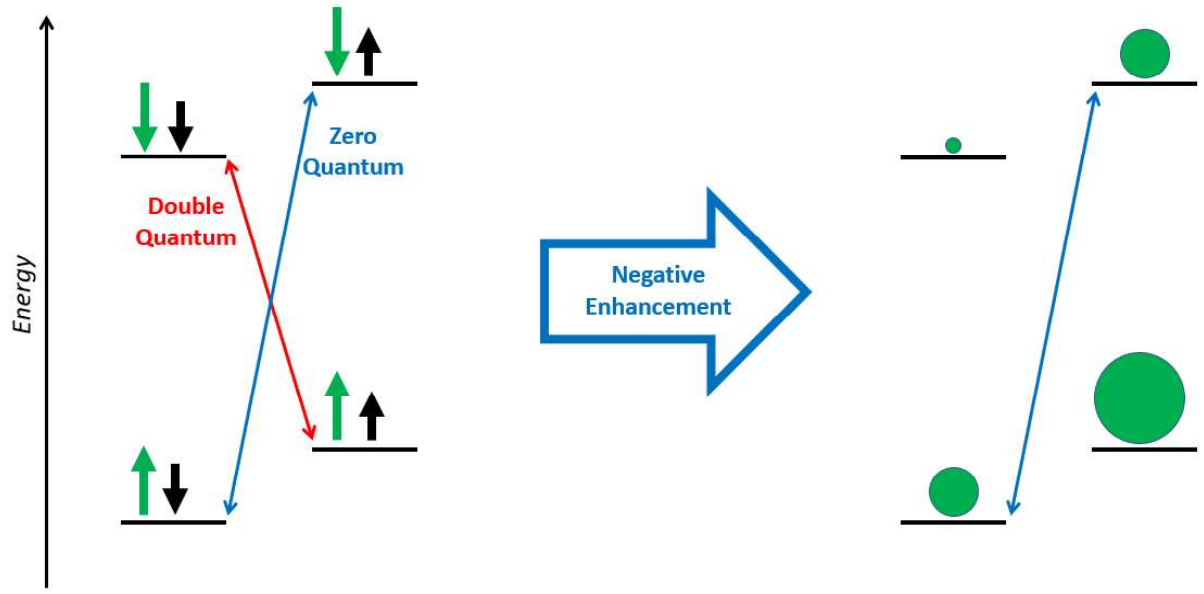

Figure 1.1: *Depiction of the solid effect, with the resulting electron polarization of the zero quantum mechanism portrayed also by the green circles whose size is qualitatively representative of the population of the energy levels. Green arrows correspond to electron spins and black arrows correspond to nuclear spins.*

If the width of the EPR lineshape exceeds the nuclear Larmor frequency of the nuclear spin targeted for polarization, then the cross effect can be exploited. The cross effect mechanism pairs the exchange (spin flip) of two electron spins with one nuclear spin. Cross effect has the benefit that the enhancement it affords scales with $1/B_0$ [8], where the solid effect enhancement scales with $1/B_0^2$ [6]. In this dissertation, the main mechanism utilized is the solid effect because the radicals used, 40 mM trityl and ^{14}N-endofullerene, both exhibit electron resonance homogeneous linewidths that are less than the Larmor frequency of the nuclei that are being polarized. However, when considering ^{13}C-enhancment using 40 mM trityl it should be noted that the base-width of the electron resonance linewidth slightly exceeds the Larmor frequency of the ^{13}C nuclei. This arises due to electron-electron interactions present in trityl clusters, which are known to occur as the trityl concentration is increased. This introduces the possibility of a combination of solid effect, cross effect, and thermal mixing for active DNP mechanisms. Thermal mixing is a mechanism that utilizes the presence of many coupled electron and nuclear spins, treating them

thermodynamically, as spin reservoirs, to establish a common value for polarization across different nuclear spins via a three-spin flip process. [9] Experiments that combine DNP build-up with nuclear spin saturation via radiofrequency pulses can determine the degree to which thermal mixing contributes to the enhancement. In the solid effect experiments presented here, with 40 mM trityl, it should be considered that cross effect, and even thermal mixing could contribute, in part, to the enhancement, given the breadth of the electron paramagnetic resonance linewidth of 40 mM trityl.

1.2.2 Dipolar Interaction

DNP is an example of exploiting an internal interaction with an external source. The connection between the electron spins and nuclear spins is the dipolar interaction. This strength of this interaction is proportional to $1/r^3$, where r is the distance separating the spins. This interaction also has the $(1 - 3\cos^2\theta)$ dependence. When involving an electron and nuclear spin, it makes up the anisotropic hyperfine interaction. In addition to its involvement in DNP transfer, this dipolar-hyperfine interaction can be used to obtain information on the structure of a sample through experiments, like electron-nuclear double resonance (ENDOR) [10]. The nuclear-nuclear dipole interaction is also used for structural determination, such as the accurate distance-determination provided by rotational echo double resonance (REDOR) [11].

The dipolar interaction carries useful structural and dynamic information, but is also a source of signal broadening. ^{1}H-decoupling with RF irradiation at the ^{1}H Larmor frequency is a common practice in MAS NMR. The NMR RF probes described here are constructed to handle enough power to adequately remove the ^{1}H's dipolar broadening effects. The frequency-agile gyrotron (microwave source) [12], whose design and construction are described here in detail, is able to mitigate the electron-nuclear dipolar interaction through the process of electron decoupling.

Electron decoupling has so far been applied to solid effect, narrow-line radicals (trityl, $^{14}N@C_{60}$) because neither the microwave power nor the range of the microwave frequency output are large enough to exert control over the broad-line, cross effect radicals [13].

1.3 Spectrometer for MAS DNP NMR

The frequency-agile gyrotron and the RF probe are two significant pieces of the DNP MAS NMR spectrometer that was designed and constructed within the lab. The entire layout is shown below in **Figure 1.s2.**

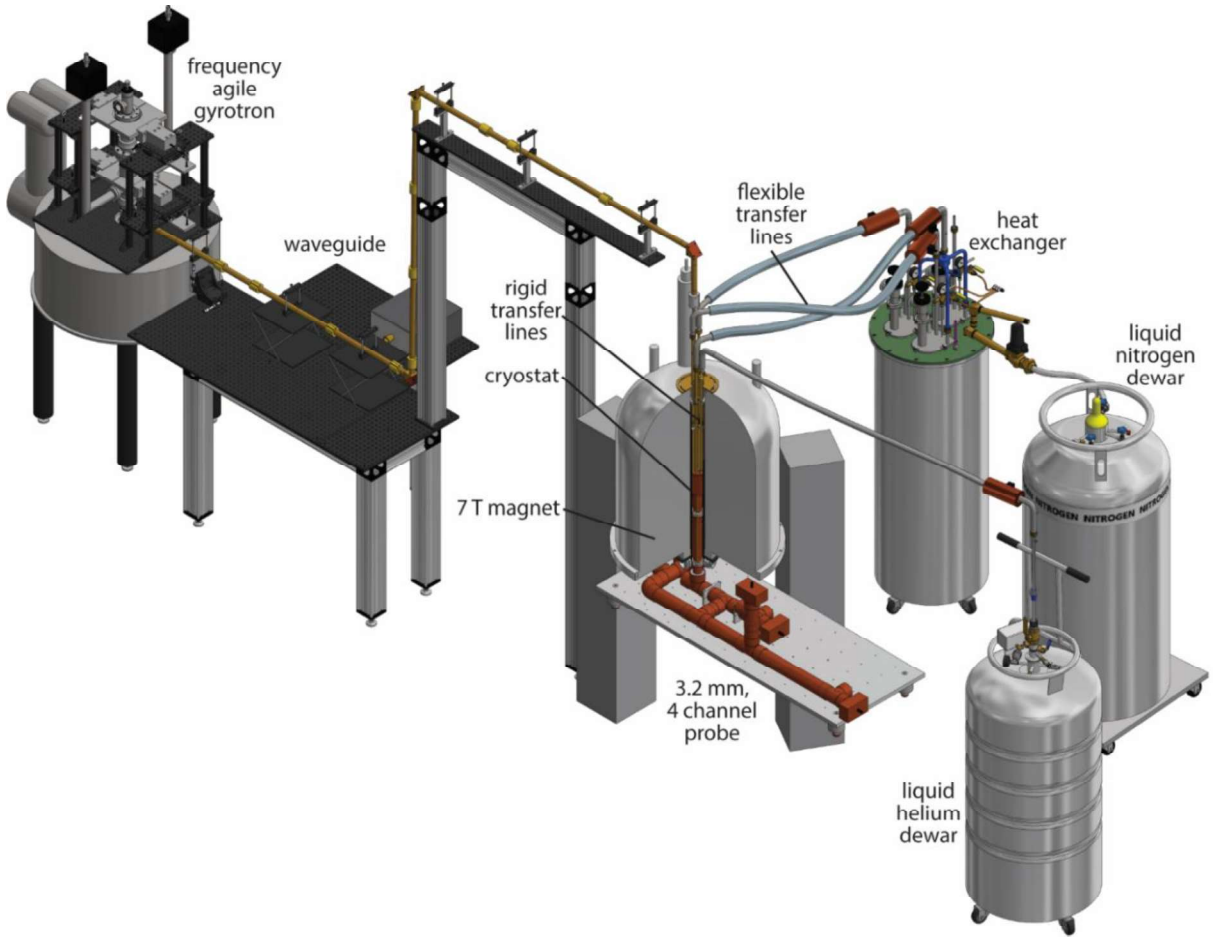

Figure 1.2*: Computer-aided design (CAD) view of the full MAS DNP NMR spectrometer. The gyrotron generates over 100 W of microwave power for DNP and electron decoupling, which is coupled to the probe through the waveguide. The system of vacuum-jacketed transfer lines, heat exchanger, and dewars allow for efficient MAS experiments at 90 K, and access to MAS experiments down to 4.2 K.*

1.3.1 Frequency-agile Gyrotron and Waveguide System

The frequency-agile gyrotron serves as the source of microwave power, generating microwaves sending the microwave beam through an overmoded waveguide to the NMR probehead, where the microwave beam is directed at the sample [12]. In a gyrotron, a beam of electrons is drawn from an AC-heated electron source with a large DC potential (10 – 15 kV). The gyrotron sits within a magnet, with a copper interaction cavity aligned in the center of the magnetic field. As the electrons travel into the magnetic field they oscillate and the electron beam compresses. At the interaction cavity, the electrons deposit kinetic energy into the cavity, where that energy is then converted into microwave irradiation. Interaction cavities can support a range of frequencies; the ones describe here have a range of several hundred MHz. The frequency-agility comes from the ability to quickly modulate that DC potential, thus changing the acceleration of the electrons, and the energy they deposit into the interaction cavity.

1.3.2 MAS NMR Probe and Transfer Line System

The MAS NMR probes used in this spectrometer are all transmission-line RF probes (Schaefer-McKay style) [14]. These probes utilize various lengths of a copper-tube coaxial line, along with variable capacitors in series and parallel to achieve a multi-resonant LC-circuit that can handle hundreds to thousands of Watts of AC power. The modular nature of these probes allows for the inclusion of multiple nuclear channels. The probehead is modular, as well. The probes presented here are able to support various diameters of cylindrical MAS systems, as well as offer the freedom to implement novel spherical MAS systems [15].

A main feature that allows for such modularity is the insert-from-the-top system of transfer lines and waveguide. In these probe designs, all spinning and cooling gas travels through vacuum-jacketed transfer lines that couple into the top of the probehead through a surrounding cryostat.

The vacuum jacketing of all cryogenic transfer lines and the NMR probehead-containing cryostat are essential to safely and efficiently conducting MAS DNP NMR experiments with cooled nitrogen at 90 K, and with liquid helium down to 4.2 K. The transfer lines, microwave waveguide, and ejection tube can all be reoriented without disturbing the probe itself, facilitating the implementation of novel MAS NMR probe designs.

1.4 Highlighting My Contributions

The work I accomplished has its foundations in instrumentation. The purpose of projects was the construction of instrumentation, itself, or an experimental result made possible through application of the instrumentation. The instrumentation that I designed, characterized, and implemented is featured in the following areas of the laboratory: MAS at 90 K and below 6 K; high-power radiofrequency performance; high-power, frequency-agile microwaves for DNP and electron decoupling; and novel MAS DNP experiments.

Experiments conducted at 90 K and below require the integration of cryogenically-cooled gases and cryogenic fluids within the magnet space and the radiofrequency circuit. Proper safety and adequate experimental efficiency both rely on the total insulation of the cryogens during transfer and the sequestration of the cryogens to the probe head during experiments. Insulation during transfer is accomplished with vacuum-insulated transfer lines. I designed and oversaw construction of a series of rigid brass transfer lines that made tight seals at the probe head and at the interface with a cryostat insert. The orientation and the path of these rigid lines depended on the purpose of their individual paths: bearing gas, drive gas, variable temperature control, sample ejection, exhaust (with return to the heat exchanger), and auxiliary exhaust. All rigid lines include a bellowed section in series with the interior tube path to accommodate for longitudinal

shrinking upon contact with cryogens. The inner and outer brass tubing is separated by a space that is evacuated by vacuum pumps through an actuator port. At the end opposite to the probehead, where the rigid lines protrude from within the magnet bore, above the top face of the magnet, are bayonet couplings that are affixed to each transfer line, save for the sample eject. These fittings are produced commercially, by Precision Cryogenics, Inc. (Indianapolis, IN), and serve to preserve the layer of vacuum insulation along the path of cryogen delivery. I designed the rigid transfer lines to accommodate these commercial fittings so that the second stage of cryogen transfer, the flexible transfer lines, could be incorporated. These flexible lines were also commercially produced by Precision Cryogenics, Inc., but I determined all the necessary dimensions to ensure that they fit within the unique geometry of the heat exchanger ports and rigid line array.

The aforementioned probehead is the location of one of the main components of the radiofrequency circuit: the inductor coil that picks up the NMR signal. Although the noise of the circuit decreases at lower temperatures, for the sake of stability and safety the only components intended to go down to cryogenic temperatures are those within the probehead space. It was my task to make design changes to improve the cryogenic performance of the four-channel transmission line probe, at the top of which sits the probehead. In addition to designing leak-tight interfaces to prevent cryogen leakage from the probehead, I introduced a room temperature nitrogen purge fixture that drastically reduces the buildup of moisture within the transmission line circuit. Over the course of use, these transmission line probes may need to be disassembled, readjusted, and reassembled; press-in Teflon capacitors wear, some capacitors may fail, solder joints can break, copper tubing can shift within couplers and lengths can change. I would routinely characterize the isolation among the channels of the transmission line probe, determine

power attenuation at different points in the path of the circuit, construct new circuit components, and characterize the performance of the different channels with standard NMR experimental techniques. This maintenance is required to keep a stable, optimal level of sensitivity for NMR experiments, which is extremely important when signal-to-noise is the metric by which results are judged.

To utilize the polarization, and thus sensitivity, afforded by unpaired electron spins with DNP, I helped design and construct multiple frequency-agile microwave sources, gyrotrons. I characterized and optimized the performance of the latest, >100 W frequency-agile gyrotron, and employed the 30 W gyrotron for electron decoupling experiments on samples containing 40 mM trityl and ^{14}N-endofullerene, and novel electron relaxation experiments with 40 mM trityl. Gyrotron construction involves exchanging, tightening, and checking on copper gasket-stainless steel flange connections; applying heating tape for an even bakeout; and ensuring that the magnetron-injection gun remains at vacuum at all times, especially during low-voltage, low-current activation. I oversaw and performed all of these tasks, most times as part or lead of a team. Installing the gyrotron within the spectrometer is a sort of ballet that involves several members of the lab and the gyrotron, as the star of the show. Rather than a reverence, at the end of the routine, the gyrotron is situated upright within its magnet, locked into an alignment cage. I have led the insertion and extraction of the last two gyrotrons that have been used in the lab. Once installed, I have conducted the slow process of increasing the heater current and anode potential to achieve electron emission from the magnetron-injection gun. I used this electron beam emission to properly align the gyrotron within the magnetic field, and then go further to achieve microwave emission with proper increase in the potential and the current. I helped develop the interface for the frequency-agility electrical connection and have characterized and

adjusted the gyrotron to achieve adequate frequency-agility. With my work spend optimizing gyrotron performance, I was able to utilize the frequency-agile microwaves to perform novel electron decoupling experiments on ^{14}N-endofullerene and 40 mM and observe the electron spin-lattice relaxation of the unpaired electron spins in 40 mM trityl.

References

[1] A. McDermott, Structure and Dynamics of Membrane Proteins by Magic Angle Spinning Solid-State NMR, Annu. Rev. Biophys. 38 (2009) 385–403. doi:10.1146/annurev.biophys.050708.133719.

[2] H. Yang, D. Staveness, S.M. Ryckbosch, A.D. Axtman, B.A. Loy, A.B. Barnes, V.S. Pande, J. Schaefer, P.A. Wender, L. Cegelski, REDOR NMR reveals multiple conformers for a protein kinase c ligand in a membrane environment, ACS Cent. Sci. 4 (2018) 89–96. doi:10.1021/acscentsci.7b00475

[3] F.A. Bovey, E.W. Anderson, D.C. Douglass, J.A. Manson, Polymer NMR spectroscopy. X. The use of H1-H1spin decoupling in the elucidation of polymer structure, J. Chem. Phys. 39 (1963) 1199–1202. doi:10.1063/1.1734413.

[4] E.O. Stejskal, J. Schaefer, J.S. Waugh, Magic-Angle Spinning and Polarization Transfer in Proton-Enhanced NMR, J. Magn. Reson. 28 (1977) 105–12. doi:https://doi.org/10.1016/0022-2364(77)90260-8.

[5] M. Ernst, A. Verhoeven, B.H. Meier, High-Speed Magic-Angle Spinning 13 C MAS NMR Spectra of Adamantane: Self-Decoupling of the Heteronuclear Scalar Interaction and Proton Spin Diffusion, J. Magn. Reson. 130 (1998) 176–185

[6] B. Corzilius, A.A. Smith, R.G. Griffin, Solid effect in magic angle spinning dynamic nuclear polarization., J. Chem. Phys. 137 (2012) 054201. doi:10.1063/1.4738761.

[7] A.A. Smith, B. Corzilius, A.B. Barnes, T. Maly, R.G. Griffin, Solid effect dynamic nuclear polarization and polarization pathways, J. Chem. Phys. 136 (2012). doi:10.1063/1.3670019

[8] V.K. Michaelis, T.-C. Ong, M.K. Kiesewetter, D.K. Frantz, J.J. Walish, E. Ravera, C. Luchinat, T.M. Swager, R.G. Griffin, Topical developments in high-field dynamic nuclear polarization, Isr. J. Chem. 54 (2014) 207–221. doi:10.1002/ijch.201300126.

[9] D. Guarin, S. Marhabaie, A. Rosso, D. Abergel, G. Bodenhausen, K. L. Ivanov, D. Kurzbach, Characterizing Thermal Mixing Dynamic Nuclear Polarization via Cross-Talk between Spin Reservoirs, J. Phys. Chem. Lett. 8 (2017) 5531–5536. doi:10.1021/acs/jpclett.7b02233.

[10] N. Weiden, H. Kaess, K. -P. Dinse, Pulse Electron Parramagnetic Resonance (EPR) and Electron-Nuclear Double Resonance (ENDOR) Investigation of N@C_{60} in Polycrystalline C_{60}, J. Phys. Chem. 103 (1999) 9826—9830. doi:10.1021/jp9914471

[11] T. Gullion, J. Schaefer, Rotational-echo double-resonance NMR, J. Magn. Reson. 81 (1989) 196–200. doi:10.1016/0022-2364(89)90280-1.

[12] F.J. Scott, E.P. Saliba, B.J. Albert, N. Alaniva, E.L. Sesti, C. Gao, N.C. Golota, E.J. Choi, A.P. Jagtap, J.J. Wittmann, M. Eckardt, W. Harneit, B. Corzilius, S. Th. Sigurdsson, A.B. Barnes, Frequency-agile gyrotron for electron decoupling and pulsed dynamic nuclear polarization, J. Magn. Reson. 289 (2018) 45–54. doi:10.1016/j.jmr.2018.02.010.

[13] E.P. Saliba, E.L. Sesti, F.J. Scott, B.J. Albert, E.J. Choi, N. Alaniva, A.B. Barnes, Electron Decoupling with Dynamic Nuclear Polarization in Rotating Solids, J. Am. Chem. Soc. 139 (2017) 6310–6313. doi:10.1021/jacs.7b02714.

[14] J. Schaefer, R.A. McKay, Multi-Tuned Single Coil Transmission Line Probe for Nuclear Magnetic Resonance Spectrometer, 1999.

[15] N. Alaniva, F. J. Scott, N. C. Golota, E. L. Sesti, E. P. Saliba, L. E. Price, B. J. Albert, P. Chen, R. D. O'Connor, A. B. Barnes, A Versatile Custom Cryostat for Dynamic Nuclear Polarization Supports Multiple Cryogenic Magic Angle Spinnint Transmission Line Probes, J. Magn. Reson. 297 (2018) 23–32.

Chapter 2:

A Transmission Line Probe and Cryogenic Delivery System for Dynamic Nuclear Polarization with Magic-Angle Spinning

Foreword

This chapter is a reproduction of the 2018 Journal of Magnetic Resonance publication, "A Versatile Custom Cryostat for Dynamic Nuclear Polarization Supports Multiple Cryogenic Magic Angle Spinning Transmission Line Probes" (*Alaniva, N.; *Scott, F. J.; Golota, N. C.; Sesti, E. L.; Saliba, E. P.; Price, L. E.; Albert, B. J.; Chen, P.; O'Connor, R. D.; Barnes, A. B. (2018) "A Versatile Custom Cryostat for Dynamic Nuclear Polarization Supports Multiple Cryogenic Magic Angle Spinning Transmission Line Probes" J. Magn. Reson. **297**. doi: 10.1016/j.jmr.2018.10.002). It is reproduced, with permission, from the Journal of Magnetic Resonance. This covers the design of radiofrequency probes for magic-angle spinning experiments at cryogenic temperatures for dynamic nuclear polarization. In order to perform experiments that make use of the hyperfine dipolar interaction between unpaired electrons and nuclei radiofrequency (RF) and microwave irradiation of sufficient strength must be coupled to the sample, and the sample must be cryogenically cooled while spinning at the magic angle. With an RF probe that is stable at cryogenic temperatures magic-angle spinning experiments from 90 K down to 4.2 K are made possible. The robustness of the RF probe also allows for

experimental boundaries to be pushed, as in the case of the rapid-acquisition sequence for direct-dynamic nuclear polarization (DNP) and electron relaxation observation. Experiments at cryogenic temperatures are safe and relatively efficient due to the system of vacuum-jacketed transfer lines and cryostat that limit the extremely low temperatures to the probe head. Current DNP techniques rely on the longer electron relaxation time at cryogenic temperatures to efficiently transfer polarization. Cryogenic cooling is also utilized to retard the motion of C_{60} fullerene and ^{14}N-endofullerene molecules, allowing for observation of structural details that would not be observable at temperatures above 90 K.

2.1 Overview

Dynamic nuclear polarization (DNP) with cryogenic magic angle spinning (MAS) provides significant improvements in NMR sensitivity, yet presents unique technical challenges. Here we describe a custom cryostat and suite of NMR probes capable of manipulating nuclear spins with multi-resonant radiofrequency circuits, cryogenic spinning below 6 K, sample exchange, and microwave coupling for DNP. The corrugated waveguide and six transfer lines needed for DNP and cryogenic spinning functionality are coupled to the probe from the top of the magnet. Transfer lines are vacuum-jacketed and provide bearing and drive gas, variable temperature fluid, two exhaust pathways, and a sample ejection port. The cryostat thermally isolates the magnet bore, thereby protecting the magnet and increasing cryogen efficiency. This novel design supports cryogenic MAS-DNP performance over an array of probes without altering DNP functionality. We present three MAS probes (two supporting 3.2 mm rotors and one supporting 9.5 mm rotors) interfacing with the single cryostat. Mechanical details, transmission line radio frequency design, and performance of the cryostat and three probes are described.

2.2 Introduction

Dynamic nuclear polarization (DNP) is a recognized method for enhancing nuclear magnetic resonance (NMR) sensitivity by transferring electron spin polarization [1–4]. Cryogenic temperatures improve DNP efficiency due to increased spin coherence time, and also increase spin polarization according to Boltzmann polarization:

$$P = \tanh\left(\frac{\gamma\hbar B_0}{2kT}\right),$$

where γ is the gyromagnetic ratio, $\hbar$ is Planck's constant divided by 2π, B_0 is the static magnetic field, k is Boltzmann's constant, and T is the temperature. Therefore, DNP is often performed at or below 100 K [5–9].

However, cryogenic sample temperatures present several logistic issues. Proper insulation is required to improve cryogen efficiency and protect the superconducting magnet. Often, vacuum-insulated transfer lines and a cryostat provide sufficient thermal isolation to thermally protect the O-rings sealing the bore tube within the magnet while also maintaining cryogenic sample temperatures [10].

Here we describe a custom DNP-NMR cryostat and a suite of probes for cryogenic magic angle spinning (MAS) experiments from 100 K to 4.2 K (**Figure 2.1**). The cryostat has seven ports accessed from the top of the magnet, each servicing a separate function: waveguide, sample input/eject, drive gas, bearing gas, variable temperature (VT) fluid, and two lines for gas exhaust. Multiple probes can be integrated to the same cryostat without fabricating additional transfer lines or waveguides. The versatile cryostat therefore greatly accelerates MAS-DNP instrumentation development.

Here we describe mechanical and cryogenic engineering details of the cryostat and also transfer lines. Designs of the waveguide and radio-frequency (RF) circuits of three transmission line probes are also presented.

2.3 Cryogenic MAS-DNP system

The MAS-DNP NMR spectrometer show in **Figure 2.1** includes a frequency-agile gyrotron [11], waveguide, fluid transfer lines, heat exchanger [5], and NMR probe.

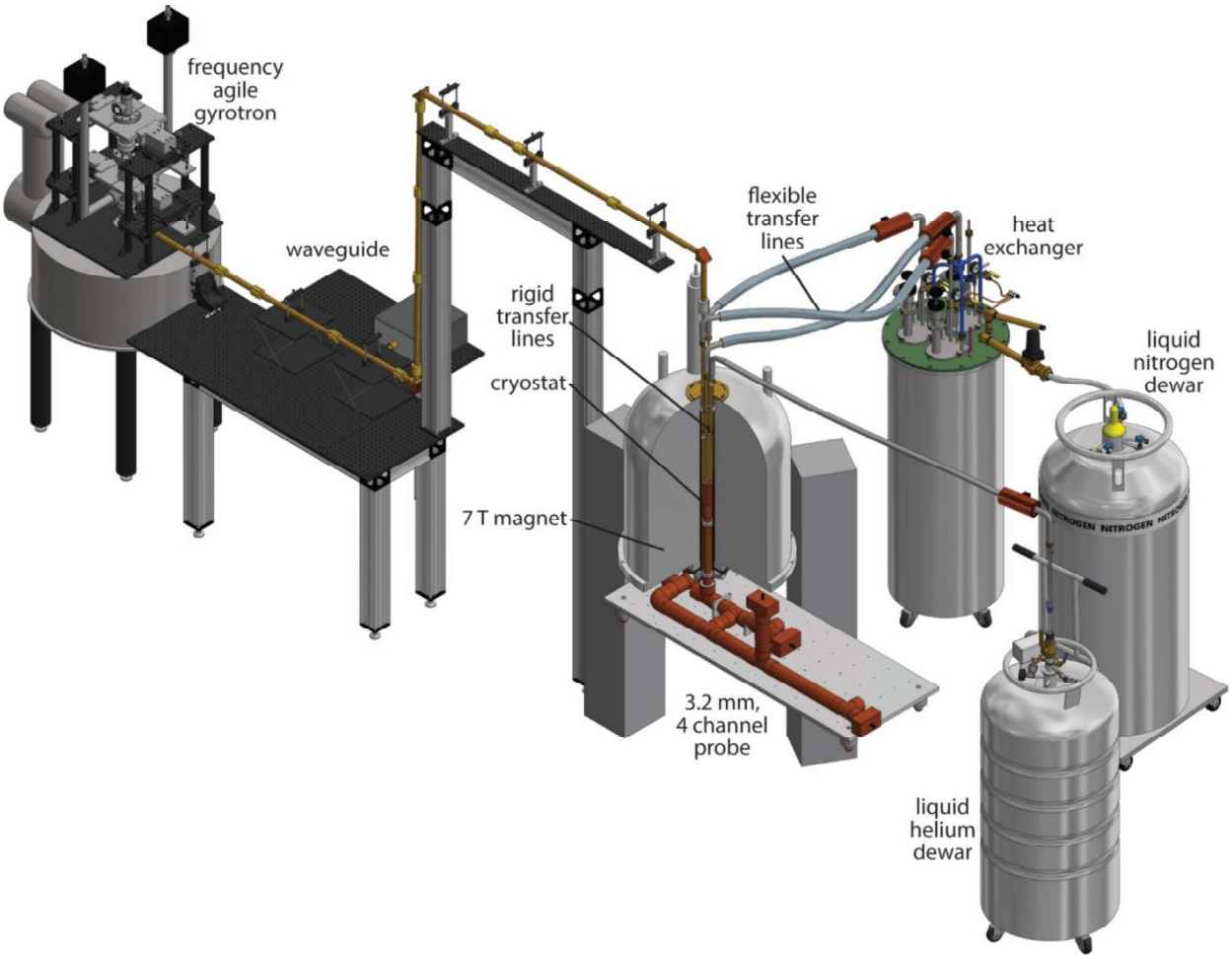

Figure 2.1: *Computer-aided design (CAD) view of the full DNP-NMR MAS spectrometer. The gyrotron generates ~30 W of microwave power for DNP, which is coupled to the probe through the waveguide. Transfer lines couple into the top of the cryostat and the probe is inserted from the bottom of the cryostat. The liquid nitrogen heat exchanger provides gas for MAS at 90 K, and MAS sample temperature of <6 K can be achieved with liquid helium cooling through the variable temperature line.*

The frequency-agile gyrotron generates microwaves for DNP, and also chirped pulses for electron decoupling [12]. Microwaves exit the gyrotron though a sapphire window and propagate through corrugated overmoded waveguide to the DNP cryostat. Transfer lines for drive and bearing gas, exhaust gas, and variable temperature fluid also mate into the top of the DNP cryostat. A cryogenic sample eject apparatus allows the exchange of samples while the probe remains in place at cryogenic temperatures [10]. A single 260 L N_2 (l) dewar supplies enough liquid nitrogen to the heat exchanger for 60 hours of continual MAS at 90 Kelvin [5]. Alternatively, 100 L of He (l) cools spinning samples to <6 K for 3 hours [13].

2.3.1 Cryostat

Probes can be exchanged within the DNP cryostat, which is mounted to the room-temperature shim stack of a 7 T magnet. Equipping the cryostat with cryogenic DNP functionality including vacuum jacketed transfer lines, waveguide, and sample exchange, reduces the experimental requirement for each probe. Probes only require RF circuitry, a stator, and optics for spinning and temperature detection. This has allowed us to fabricate three transmission line probes for a fraction of the resources typically required for cryogenic MAS DNP instrumentation. A Tecmag console generates RF pulses for control of ^{1}H, ^{31}P, ^{13}C, and ^{15}N nuclear spins, and also voltage profiles for chirped microwaves pulses and electron spin control (Tecmag, Inc, Houston, TX).

The cryostat protects the magnet and helps establish cryogenic sample temperatures (**Figure 2.2**) [14]. Introducing cryogens into the warm bore of a superconducting magnet can result in a quench if the O-rings sealing the magnet bore tube freeze. A vacuum insulated bronze cryostat provides the necessary protective thermal insulation between the sample chamber and magnet bore, while conserving valuable space. The cryostat is 0.90 m long and extends 0.86 m into the magnet bore. O-ring seals at the interface with the transfer lines (within the magnet bore) and the

interface with the probe stack (below the magnet) isolate the inner space of the cryostat. The cryostat is inserted and mounted from below the magnet, and accepts the probe from beneath and transfer lines from above.

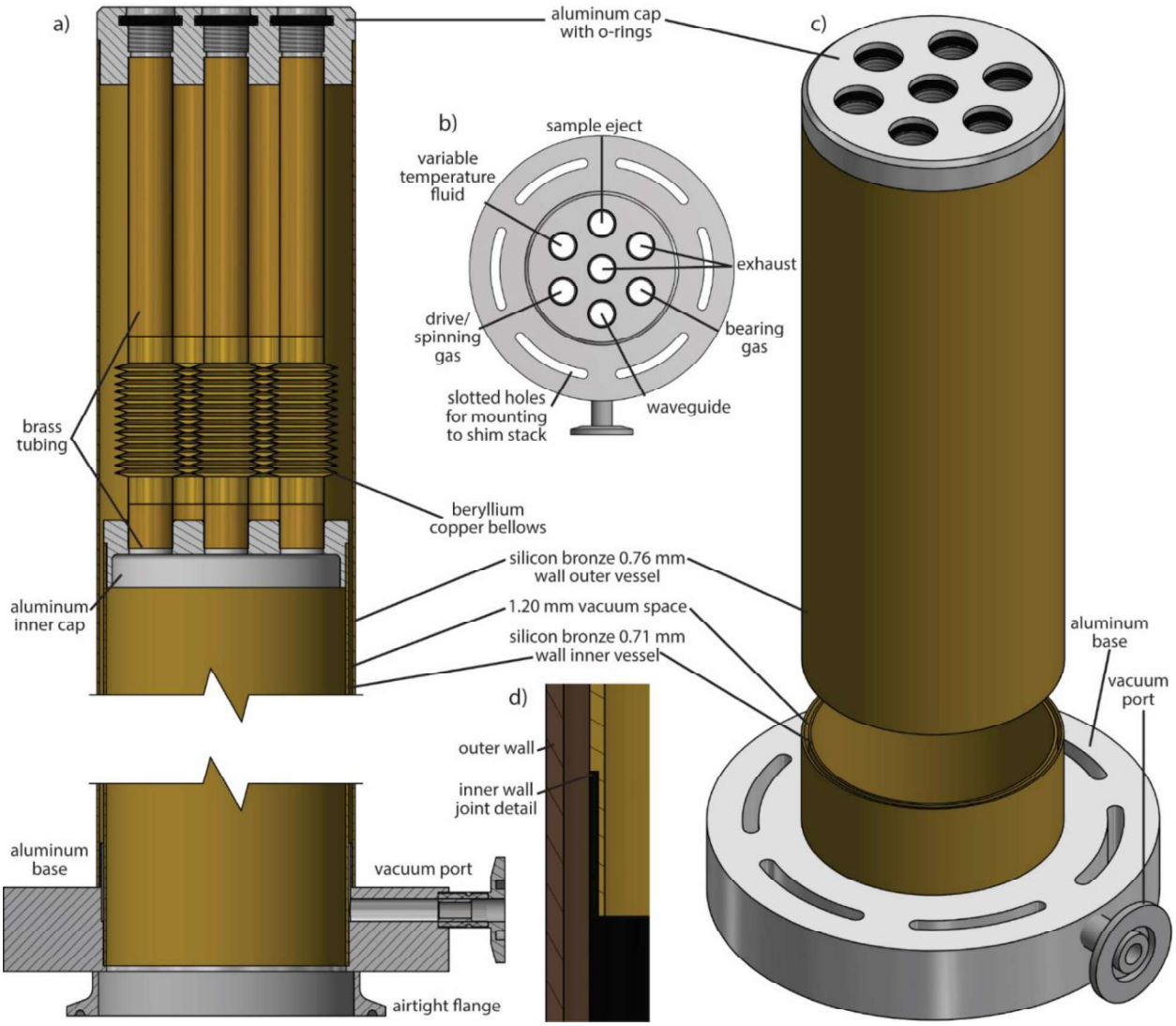

***Figure 2.2**: **a)** CAD section view of cryostat. **b)** Top view CAD of cryostat indicating the location of transfer lines for the probe containing the 3.2 mm rotor. **c)** Isomet-ric CAD of cryostat. **d)** Wall detail to show interlocking cryostat wall joints. All seals were made with cryogenic-grade epoxy.*

Inner and outer cryostat vessel walls are 0.71 and 0.76 mm thick bronze, respectively. The vessels are aligned concentrically with a 1.20 mm gap evacuated to <5 x 10^{-6} Torr (**Figure 2c).** The vessels were machined from 3" round bar C65500 silicon bronze. Silicon bronze results in a

homogenous magnetic field for high-resolution NMR, and can also be machined to thin-walls to maximize interior volume [14]. Due to machining restrictions, the inner vessel is constructed in three sections and the outer vessel in four sections, with sections cut to overlap as shown in **Figure 2.2d** to align the joined sections along the central axis. Beryllium copper bellows (Mini-Flex Corporation, Ventura, CA) are included into each port to accommodate thermal contraction of the inner vessel. The vessels and aluminum cap and base were fabricated in the Washington University in Saint Louis (WUSTL) chemistry department machine shop and sent to Precision Cryogenics, Inc. (Indianapolis, IN) for assembly with cryogenic epoxy.

The cryostat has an internal diameter of 68.3 mm to accommodate probes, and the aluminum base is attached to the shim-stack under the magnet. A tri-clover type flange mates to a collar on the NMR probe stack to provide a tight seal. Seven smaller threaded ports in the top aluminum cap allow gases (bearing, drive, VT, exhaust), microwaves, and NMR samples to enter and exit the NMR probe (**Figure 2.2b**). The ports are equally sized so that transfer lines can be rearranged into any probe configuration. To seal the inner space of the cryostat O-rings, (0.4375" inner diameter, Buna-N, McMaster-Carr, Elmhurst, IL) surround each line and are compressed with a brass plate mirroring the port pattern of the cryostat (**Figure 2.3**). Rods are threaded into a brass anchor plate fixed to the top of the magnet to compress the O-rings (**Figure 2.3**). This anchor plate has channels that allow room temperature air to circulate at the top of the magnet.

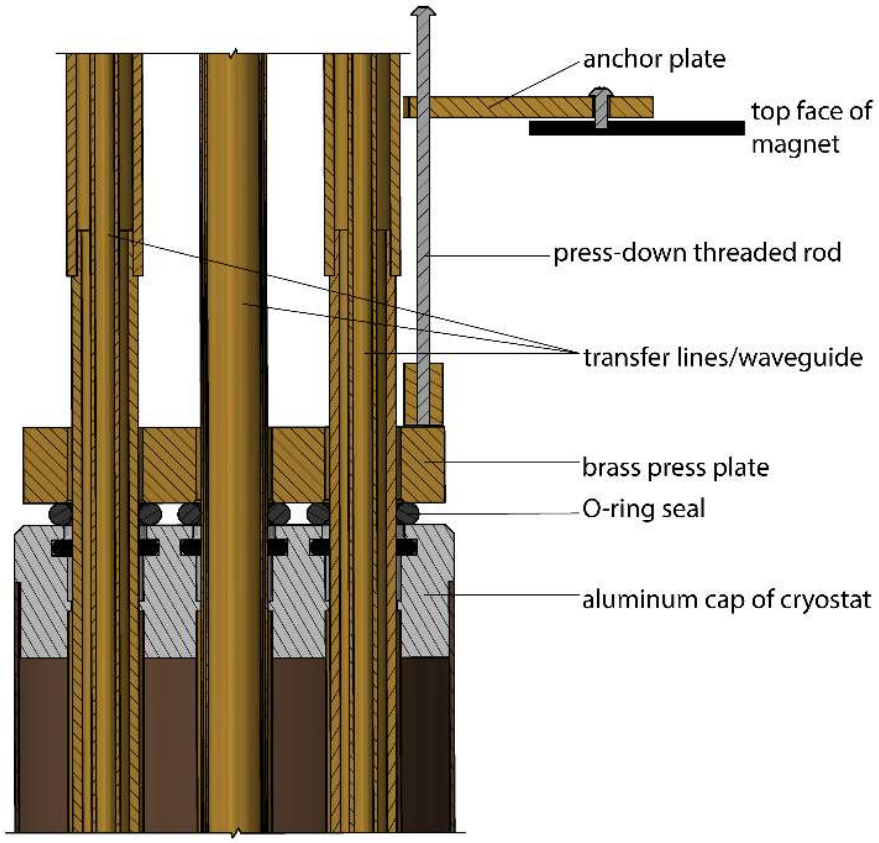

Figure 2.3 *Section view detailing the top of the cryostat with brass press plate and transfer lines installed.*

2.3.2 Transfer Lines for Cryogenic Fluid

The seven ports on the top of the cryostat are identical to allow rearrangement of the transfer lines and waveguide and adaptation to different probe configurations. Vacuum-jacketed transfer lines provide excellent thermal isolation for cryogen delivery to the sample space. The rigid transfer lines mate into the cryostat and are connected to flexible vacuum-jacketed lines via bayonet connections (Precision Cryogenics, Inc.). The flexible lines supply gases to and from the heat exchanger. (**Figure 2.4**).

The bearing and drive gas, VT fluid, and exhaust ports each have their own transfer line, which allows for fine temperature and flow control of different cryogenic channels. The VT line can

also transfer liquid helium, while drive and bearing lines transfer helium or nitrogen gas [13]. Two exhaust lines are used: one to carry cryogens through counterflow coils in the heat exchanger to act as a refrigerant, and the other to reduce backpressure during liquid helium experiments, thus improving spinning stability. The rigid transfer lines are constructed from brass tubing. The vacuum chamber is sealed at the bottom with a brass plug and extends through the bayonet connector to provide insulation at the rigid and flexible transfer line interface. A port soldered to the outer jacket with an actuator sealed by two O-rings is used to access the vacuum space (by removing an O-ring-sealed port plug), which is evacuated to $<10^{-4}$ Torr through a flexible thin-walled hose connected to a vacuum manifold. Multiple ports on the vacuum manifold allow all transfer lines to be continually connected, pressure monitored, and evacuated as needed, to reduce downtime of the instrument (see photo in Appendix).

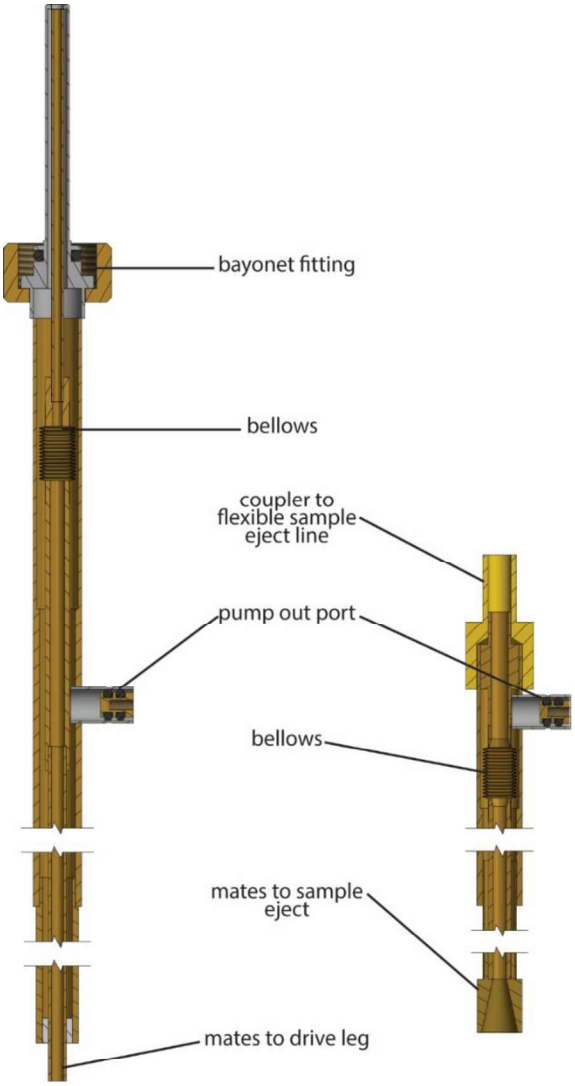

***Figure 2.4**: CAD section view of drive gas line (left) and sample eject line (right). The vacuum space between the inner and outer brass tubes is kept in the order of 10-4 Torr. The drive gas line delivers cryogenic gas to spin the rotor; the sample-eject inner path is modified to allow for rotor transfer in and out of the probe space.*

2.3.3 Transmission-line Circuits for Cryogenic MAS-NMR

Vacuum-insulated fluid transfer lines and the microwave waveguide descend from the top of the cryostat to the center of the magnet bore, where they couple to the probehead. This probehead contains the stator body, which in turn

contains the sample coil. The sample coil is electrically connected to the inner and outer conductors of a transmission line. [18,19]. A main advantage of transmission line circuit is the remote location of the tuning and matching capacitors, which allows for easy, room temperature access while the sample is maintained at cryogenic temperatures [20,21]. Impedance matched to 50 ohms is necessary for efficient power delivery to the sample and subsequent signal detection. Proton decoupling and multi-resonance manipulation are essential for most modern NMR experiments. Here we describe two probes designed for ^{1}H and ^{13}C experiments (3.2 and 9.5 mm) and a third 3.2 mm probe for ^{1}H, ^{13}C, ^{31}P, and ^{15}N experiments.

The coincident manipulation and detection of different nuclear spins requires electrical isolation between channels. **Figure 2.5** shows the complete circuit schematic. The elements that comprise both two-channel probes are shown in black and the additional components for the four-channel probe are shown in orange. **Table 2.1** lists the capacitor values of all probes, and **Tables 2.2-2.4** report the isolation values between the various probe channels.

Three probes were built at WUSTL with a combination of commercially available and custom-machined parts. Transmission lines consist of an inner conductor centered within the outer conductor using Teflon spacers. The inner conductor is made of type K ¾" copper pipe cut to length and fitted with copper shims, and the outer conductor is constructed of type M 2½" copper pipe. All outer conductor couplings are cut in half for easy access to the center conductor and secured with 316 stainless steel hose clamps.

Isolation of the highest frequency ^{1}H channel is primarily achieved with a current node. A length equivalent to ¾ of the 300 MHz ^{1}H wavelength is connected between ground and the ^{1}H current node to provide isolation from the ^{1}H channel to the lower frequency channels (**Figure 2.5d**). A copper cap on the elbow connecting the vertical transmission is capacitively coupled to the grounded outer conductor through a variable plate to allow fine adjustment of the ^{1}H node. (**Figure 2.5g**). Lower frequency channels are isolated from higher frequency channels using in-line capacitors such as those shown in **Figure 2.5h** and **Figure 2.5i**.

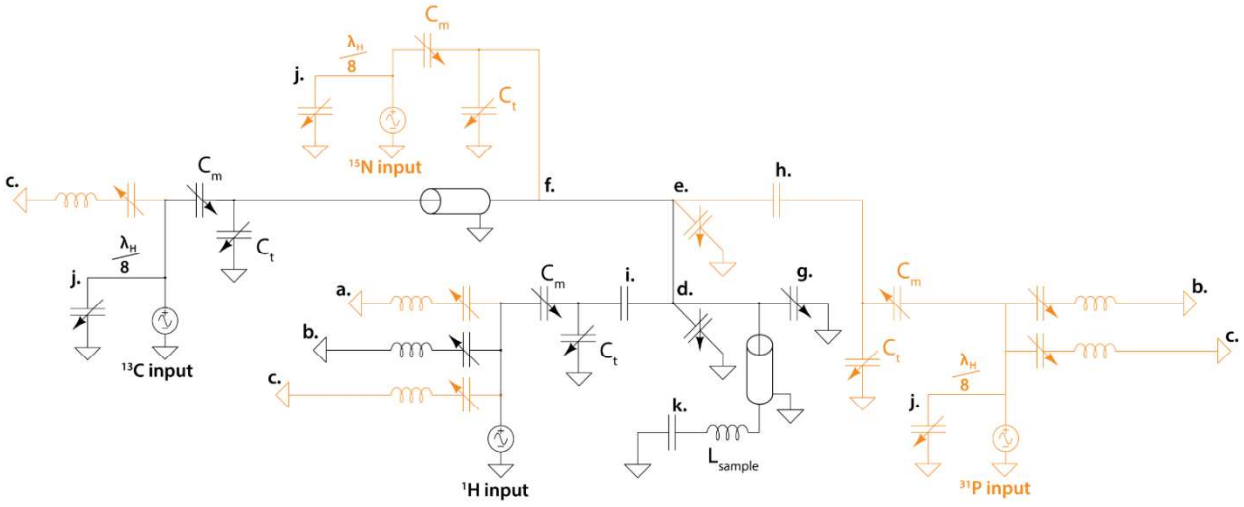

Figure 2.5*:Circuit schematic of the radio frequency (RF) probes. Shown in black are the components that make up a two-channel ^{1}H, ^{13}C probe. The components shown in orange are those that must be added for a four-channel ^{1}H, ^{31}P, ^{13}C, ^{15}N probe.* ***a.)*** *^{31}P RF trap.* ***b.)*** *^{13}C RF trap.* ***c.)*** *^{15}N RF trap.* ***d.)*** *^{1}H current node with phosphorus node adjust capacitor.* ***e.)*** *^{31}P current node with ^{13}C node adjust capacitor.* ***f.)*** *^{13}C current node.* ***g.)*** *^{1}H current node adjust capacitor.* ***h.)*** *In-line capacitor.* ***i.)*** *Teflon disk capacitor* ***j.)*** *One-eighth ^{1}H wavelength and variable capacitor for ^{1}H trap* ***k.)*** *ATC chip capacitor.*

For improved isolation, LC traps are added into the rectangular boxes housing the tuning and matching capacitors (**Figure 2.6**) (Jennings, Memphis, TN). These LC traps contain an adjustable capacitor to fine-tune the isolation. A chip capacitor in the probehead between the sample coil and ground results in improved RF transmission (American Technical Ceramics Corp, Huntington Station, NY).

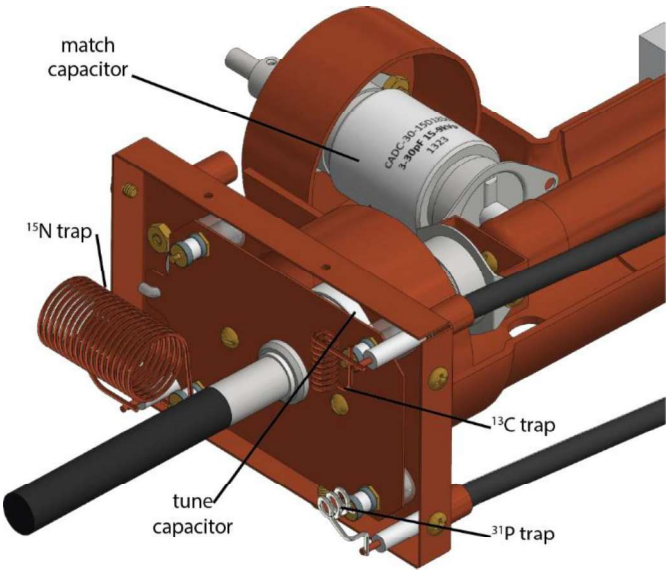

***Figure 2.6**: CAD detail view of the tune and match box showing tune and match capaci-tors and three LC traps terminating in ¼ wavelength cables to ground.*

Due to the cryogenic temperatures present at the probehead in most DNP-NMR experiments, a 0.33 m section of the inner and outer conductors in the vertical stack leading to the NMR coil is composed of 316 stainless steel as a thermal break, followed by 0.1 m of copper to prevent magnetic field distortion near the NMR sample. The inner surface of the stainless steel outer conductor and the outer surface of the stainless steel inner conductor are coated; first in gold to activate the surface, then 1.27 μm of silver for electrical conduction, followed by another gold coating to prevent oxidation of the silver. The silver coating on stainless steel allows electrical conduction through the probe stack while preserving thermal insulation [10].

Probeheads housing stators for 3.2 mm and 9.5 mm cylindrical rotors have the same circuitry but differ in fluid delivery configurations and microwave coupling schemes.

The stator for the 3.2 mm probehead was custom machined from Kel-F in the Washington University in St. Louis machine shop with the addition of ceramic bearings and a brass drive cup (Revolution NMR, Fort Collins, CO). A Kel-F coil block attached to the bottom of the stator secures the coil leads and fiber-optics for spinning detection.

The NMR coil (100 nH, 5 turns, 5.7 mm long, 18 gauge copper wire) is mounted to the inner conductor with a set screw and an ATC chip capacitor that is grounded to the outer conductor (**Table 2.1**). Teflon in the probehead electrically isolates the inner and outer conductors.

Table 2.1: *Capacitor value summary for all probes*

Capacitor	3.2 mm rotor 4-channel probe	3.2 mm rotor 2-channel probe	9.5 mm rotor 2-channel probe	Description
a.	1-14 pF	--	--	*Variable capacitor in ^{31}P trap*
b.	1-14 pF	1-14 pF	1-14 pF	*Variable capacitor in ^{13}C trap*
c.	1-14 pF	--	--	*Variable capacitor in ^{15}N trap*
d.	5-10 pF	--	--	*Teflon cap + air gap at ^{1}H node*
e.	5-10 pF	--	--	*Teflon cap + air gap at ^{31}P node*
g.	0.3-3.3 pF	0.8-8.8 pF	0.8-8.8 pF	*Proton node adjust, end cap*
h.	25 pF	--	--	*^{31}P in-line capacitor*
i.	10 pF	10 pF	10 pF	*Teflon disk capacitor*
j.	1-14 pF	1-14 pF	1-14 pF	*Variable capacitor for ^{1}H trap*
k.	220 pF	220 pF	110 pF	*Chip capacitor*
C_m	3-30 pF	3-30 pF	3-30 pF	*Matching capacitor*
C_t	3-30 pF	3-30 pF	3-30 pF	*Tuning capacitor*

The back leg (**Figure 2.7a**, green) for bearing gas is machined from Kel-F. The yellow leg in the foreground contains channels that deliver drive gas and VT fluid to the stator and was 3D printed from ABS-like plastic by 3D Systems (Rock Hill, SC). A sample eject piece over the stator opening allows for cryogenic sample exchange within minutes (3D Systems) [10]. Connections from the transfer lines to the probehead can-top and the stator legs are airtight. The waveguide irradiates the sample rotor perpendicular to its spinning axis at an electron Rabi frequency of 0.38 MHz with 5 W of microwave irradiation [22]. The maximum spinning frequency of this

probe is 20 kHz ± 5 Hz with nitrogen gas at room temperature. This same frequency is attainable at 90 K and below 6 K when utilizing ultra-pure, cooled helium gas (77 K), but the limit falls to 10 kHz when using nitrogen gas at 90 K.

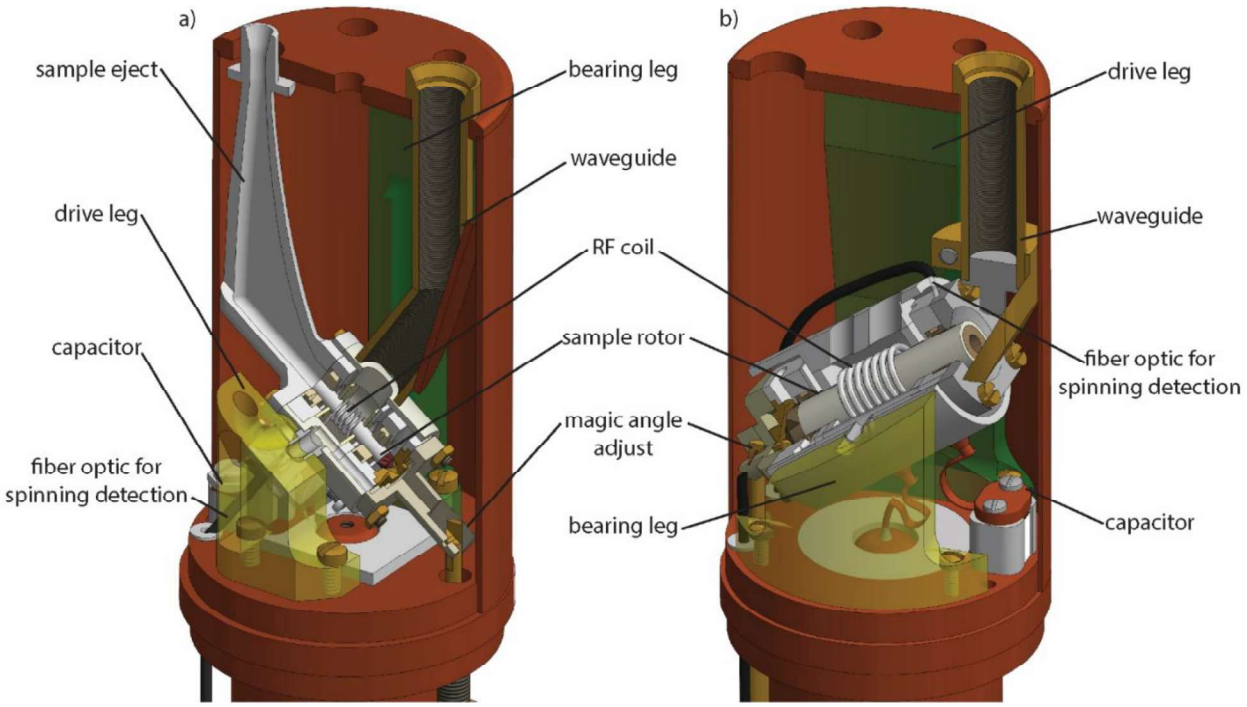

***Figure 2.7**: CAD detail view of probehead for a) 3.2 mm OD rotor and b) 9.5 mm OD rotor.*

The stator for 9.5 mm OD cylindrical rotors (**Figure 2.7b**) is larger, yet must reside in the same volume probehead as the 3.2 mm stators housing 3.2 mm OD cylinders, leaving insufficient space for a sample eject. Stator bearings, drive cup, and rotor were purchased from Revolution NMR, and 3D Systems 3D printed the drive and bearing legs using ABS-like plastic. The coil leads are a flat copper ribbon; one side of the ribbon is soldered to the inner conductor and the other lead is clamped in line with a 110 pF chip capacitor to ground. The coil inductance is 630 nH (7 turns, 14.3 mm, 18-gauge copper wire). The stator orientation is reversed such that the drive and bearing lines are transposed and the exhaust line goes through the port previously used for the sample eject line. A lens is added before the final waveguide mirror to focus the Gaussian

beam, with the mirror directing the microwaves along the rotor's spinning axis. The electron Rabi frequency using this on-axis microwave coupling method and an opposing metallic reflector was 0.34 MHz with a 5 W input, as calculated with an electromagnetic simulation package within Ansys HFSS (Canonsburg, PA) [23]. The maximum spinning frequency for the rotor in this probe is 5 kHz +/- 10 Hz at room temperature. When cooling the sample to 120 K with chilled nitrogen gas the maximum spinning frequency is 2 kHz.

The four-channel NMR probe with 3.2 mm OD cylindrical rotors (**Figure 2.8a,d**) has been used in a variety of experiments [5,11–13,24]. The combination of ^{1}H, ^{31}P, ^{13}C, and ^{15}N channels allows investigation of biological systems, with ^{13}C and ^{15}N isotopes found in proteins and used for a variety of labeled and unlabeled 2D-NMR experiments. ^{31}P is also a useful biological isotope found in phospholipid head groups in cellular membranes, while the ^{1}H channel, which can be used for detection or 2D experiments, is most often used for cross-polarization and subsequent decoupling. Isolation values for this probe are shown in **Table 2.2**.

Table 2.2: *Isolation values and nutation frequencies of four-channel probe with 3.2 mm OD rotor. Power value used for nutation frequency is given in the last row. Proton decoupling is conducted at 83 kHz for no more than 40 ms at room temperature and cryogenic temperatures.*

Transmitting→ Receiving↓	^{1}H	^{31}P	^{13}C	^{15}N
^{1}H	--	-60 dB	-60 dB	-60 dB
^{31}P	-54 dB	--	-67 dB	-43 dB
^{13}C	-52 dB	-37 dB	--	-34 dB
^{15}N	-58 dB	-50 dB	-38 dB	--
Nutation Frequency	222 kHz	125 kHz	154 kHz	181 kHz
Power from amplifier	800 W	900 W	820 W	910 W

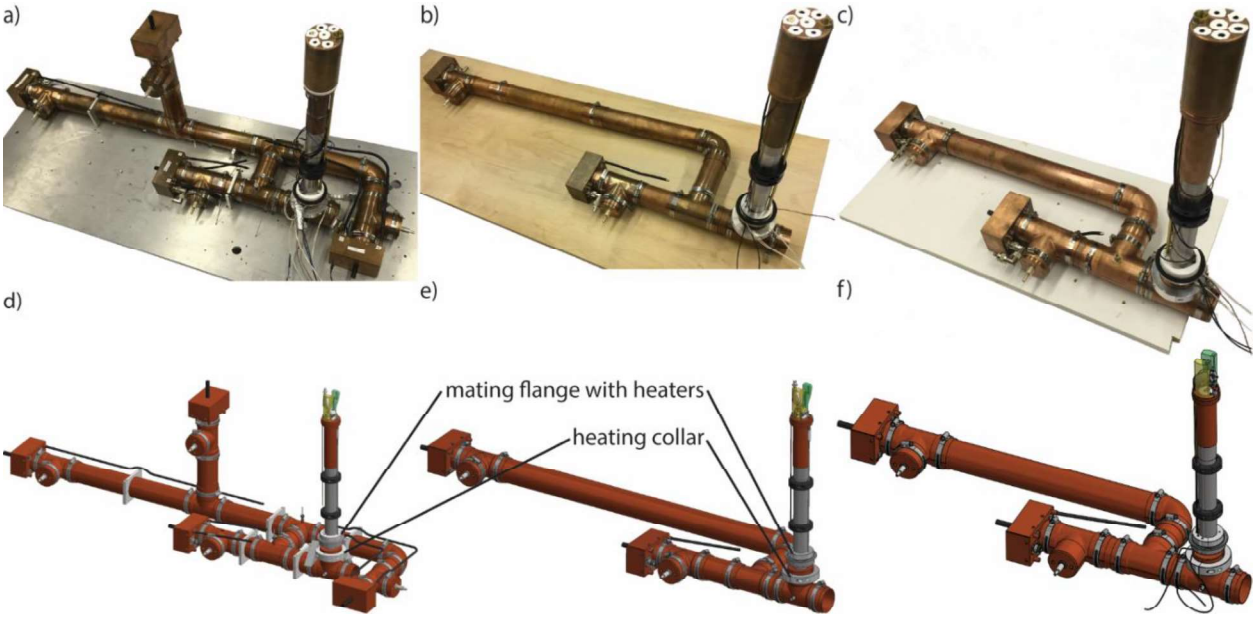

***Figure 2.8**: Photographs of **a.)** 4-channel probe with 3.2 mm OD rotor, **b.)** 2-channel probe with 3.2 mm OD rotor, and **c.)** 2-channel probe with 9.5 mm OD rotor. CAD views of **d.)** 4-channel probe with 3.2 mm OD rotor, **e.)** 2-channel probe with 3.2 mm OD rotor, and **f.)** 2-channel probe with 9.5 mm OD rotor with can top removed.*

The two-channel version of the 3.2 mm OD rotor probe (**Figure 2.8b,e**) is capable of a variety of DNP-NMR experiments on biological samples and materials. ^{13}C capability is useful for fully or partially isotopically labelled proteins. The ^{1}H channel is used for cross polarization and proton decoupling for increased resolution. This probe can be interchanged quickly for the four-channel probe to further customize either probe. ^{13}C nutation frequency (**Table 2.3**) is slightly higher for the two-channel probe, but the ^{1}H nutation frequency is nearly halved, indicating that less power is available for decoupling.

***Table 2.3:** Isolation values and nutation frequencies of two-channel probe with 3.2 mm OD rotor. Power value used for nutation frequency is given in the last row. Proton decoupling is conducted at 83 kHz for no more than 40 ms at room temperature and cryogenic temperatures.*

Transmitting → Receiving↓	^{1}H	^{13}C

^{1}H	--	-54 dB
^{13}C	-36 dB	--
Nutation frequency	125 kHz	167 kHz
Power from amplifier	800 W	820 W

The two-channel probe built for 9.5 mm OD cylindrical rotors (**Figure 2.8c,f**) is capable of the carbon–proton experiments described above but with a 600 µL sample size, 17-times that of the 3.2 mm rotor. The ^{13}C nutation frequency in the 9.5 mm rotor probe is 71 kHz at 600 W input power (**Table 2.4**). At 820 W, the ^{13}C nutation frequency is 97 kHz, i.e., 1.72-times lower than the 167 kHz nutation frequency of the 3.2 mm two-channel probe but providing an overall gain of ~10-times NMR sensitivity for these much larger samples.

Table 2.4: *Isolation values and nutation frequencies of two-channel probe with 9.5 mm OD rotor. Power value used for nutation frequency is given in the last row. Proton decoupling is conducted at 30 kHz for no more than 40 ms at room temperature and cryogenic temperatures.*

Transmitting → Receiving↓	^{1}H	^{13}C
^{1}H	--	-68 dB
^{13}C	-46 dB	--
Nutation frequency	40 kHz	71 kHz
Power from amplifier	800 W	600 W

This sensitivity gain can be exploited for inexpensive samples with low levels of isotopic labeling such as in naturally abundant whole cells. Alternatively, the large rotor can be used for a secondary Teflon microwave lens leading into a smaller sample volume. This strategy is

particularly advantageous for pulsed DNP and electron decoupling research because of the drastically increased electron Rabi frequency and homogeneity in small samples (as small as 3 μL in preliminary calculations). Overall, the large rotor contained in the 9.5 mm MAS probe allows the flexibility to use large sample sizes for samples dilute in isotopic labels and increased electron Rabi frequency for pulsed DNP.

2.4 Mechanical and Cryogenic Engineering

Two sets of heating collars are integrated into each of the three probes introduced above. The cryostat-mating collar contains two cartridge heaters inserted into the body of the collar from the underside (OMEGA Engineering, Inc, Norwalk, CT). This collar is clamped around the 316 stainless steel vertical stack of the probe and compresses an O-ring to seal the cryostat-probe connection below the magnet (**Figure 2.2, 2.1**). There is an additional heating collar mounted around the vertical portion of the copper outer conductor at the final three-way joint, which mates to the vertical stack. The heating elements maintain ambient temperature of the outer conductor of the transmission lines located below the magnet bore. This heating collar is crucial for preventing ice formation within the transmission lines and probe de-tuning. To further combat ice formation, high-flow dry air flows around the cryostat-vertical stack interface. A high flow of room temperature nitrogen gas is also injected into the space between inner and outer conductors at the center of the probe three-way joint directly under the magnet bore.

2.4.1 MAS Adjustment

The ability to adjust the angle of the sample spinning axis relative to the main magnetic field is a necessity in MAS NMR. This is achieved using a threaded rod to push and pull one end of the sample housing as it pivots about its bearing and drive gas import channels. This simple solution requires modification for experiments at cryogenic temperatures.

When spinning with gases at 80 K and cooling with fluids down to 4.2 K, the stator shrinks, which can alter the sample angle set at room temperature. It is crucial that the probe design allows for magic angle adjustment at these temperatures. The main body of the magic angle adjustment rod is a 0.5” OD brass rod with threading at the end to mate with threading in the probehead base. A freely rotatable brass end-piece attaches to an extension of the stator body. The rod adjust then extends downward to protrude below the underside of the probe stack heater/cryostat coupler. A Gore-Tex plug is fixed to the rod above the interface between the rod adjust and the top side of this stack heater. The plug prevents any potential cryogen leak through the small clearance between the rod adjust and the through hole in the stack heater while maintaining free rotation of the rod adjust. This design allows for magic angle adjustment at cryogenic temperatures and ensures integrity of the magic angle during DNP-MAS.

2.4.2 Temperature measurement of MAS at 4.2 – 6 K (with and without microwaves)

Attaining sub-6 K temperatures requires application of liquid helium to the center of the sample as it spins in the stator. To accurately determine the temperature, a Cernox temperature sensor is inserted at the interface between the stator body and the VT outlet. Lake Shore Cryotronics, Inc. calibrated the temperature sensor to a temperature of 1.2 K within a magnetic field of 7 T, matching laboratory conditions. This temperature sensor reports temperatures of 4.2 – 5.0 K without microwave irradiation and 5.3 – 6.0 K with microwave irradiation. This experimental data, together with fluid dynamics simulations [13], shows that these MAS-DNP experiments with liquid helium VT fluid are conducted at sample temperatures between 4.2 and 6 K.

2.4.3 Quality factor at 298 K and 6 K

In NMR, the quality factor Q indicates the power loss within the sample coil at a given frequency. $Q = \omega L/R$, where R is the effective resistance of the inductor coil, ω is the operating frequency, and L is the effective inductance of the coil [25]. A higher Q factor indicates that higher RF fields can be generated in the sample, with a reciprocal gain in sensitivity. **Figure 2.9** shows a comparison of resonant tune/match obtained using a Vector Network Analyzer (SDR-Kits, Melskam, Wilts, UK) at 300.179 MHz of the 3.2 mm, four-channel transmission line probe at room temperature (296 K), 90 K, and 6.2 K. Q at 296 K=390, Q at 90 K=790, and Q at 6.2 K=880. These resonances were obtained after re-optimization of tune and match at each temperature. As the sample temperature decreases, the Q factor of the inductor at 300.179 MHz increases. This increase in Q factor at the proton frequency allows for decoupling at lower power from the high-power amplifier, or, in turn, for high ^{1}H decoupling (Tomco, Stepney, South Australia).

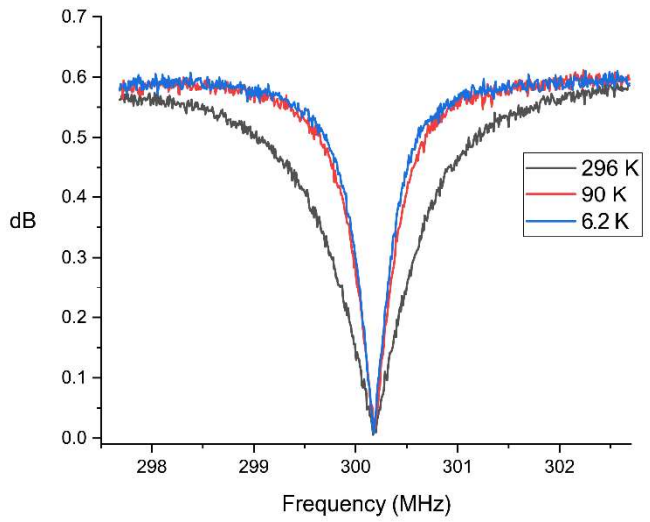

***Figure 2.9**: Magnitude plots of the amount of reflected power (the S11 signal using a Vector Network Analyzer) in the proton circuit of the 3.2 mm, four-channel probe at sample temperatures of 296 K (black), 90 K (red), and 6.2 K (blue). The impedance of the channel is matched to 50 ohms at 300.179 MHz, and the quality factor of this circuit increases with decreasing temperature at the sample coil. These plots were generated with a Vector Network Analyzer. Q at 296 K = 390; Q at 90 K = 790; and Q at 6 K = 880.*

2.5 Conclusions and Outlook

The adaptable nature of this cryostat-transfer line system allows for novel MAS-DNP NMR probes to be constructed and implemented at a reduced cost [26]. The vacuum-jacketed cryostat protects the NMR magnet during cryogenic experiments, and vacuum-jacketed transfer lines and

a sample eject line increase the efficiency of MAS-DNP experiments conducted below 6 K. This system allows for the manufacture, modification, and testing of stator design, microwave delivery, and probe circuitry with relative ease.

The customizable nature of the presented NMR probes allows for future development. One proposed addition to the two-channel 3.2 mm probe is a ^{19}F channel (282.231 MHz). A $\lambda_F/4$ open-circuit transmission line (JS trap) can be implemented to isolate ^{19}F frequency from going into the ^{1}H channel [27]. ^{19}F is a desirable isotope for NMR due to its stability, high natural abundance, and high NMR sensitivity. It is suitable for physiological and pharmacological studies *in vivo* by virtue of its bioorthogonal nature. ^{19}F has previously been integrated into PKC activating ligands for REDOR distance measurements to reveal multiple conformers [28]. The 4-channel 3.2 mm rotor probe is also compatible with a ^{2}H channel for additional REDOR and ^{2}H-^{13}C and ^{2}H-^{15}N correlation experiments [29]. Flexibility in available probes also allows for future instrumentation development such as sample rotors of different geometries able to spin at frequencies >20 kHz. The DNP cryostat described in this manuscript facilitates innovation in future MAS-DNP probes and other instrumentation.

2.6 Acknowledgements

Grants from the NSF-IDBR (CAREER DBI-1553577), the NIH Director's New Innovator Award from the National Institutes of Health (DP2GM119131), and a Camille Dreyfus Teacher-Scholar Award supported this work. We thank Jacob Schaefer and Gregory Potter for helpful discussions.

References

[1] A.S. Lilly Thankamony, J.J. Wittmann, M. Kaushik, B. Corzilius, Dynamic nuclear polarization for sensitivity enhancement in modern solid-state NMR, Prog. Nucl. Magn.

Reson. Spectrosc. 102–103 (2017) 120–195. doi:10.1016/j.pnmrs.2017.06.002.

[2] M. Renault, S. Pawsey, M.P. Bos, E.J. Koers, D. Nand, R. Tommassen-Van Boxtel, et al., Solid-state NMR spectroscopy on cellular preparations enhanced by dynamic nuclear polarization, Angew. Chemie - Int. Ed. 51 (2012) 2998–3001. doi:10.1002/anie.201105984.

[3] L.R. Becerra, G.J. Gerfen, R.J. Temkin, D. Singel, R.G. Griffin, Dynamic nuclear polarization with a cyclotron resonance maser at 5 T, Phys. Rev. Lett. 71 (1993) 3561–3564. doi:10.1103/PhysRevLett.71.3561.

[4] A. Lesage, M. Lelli, D. Gajan, M.A. Caporini, V. Vitzthum, P. Miéville, et al., Surface enhanced NMR spectroscopy by dynamic nuclear polarization., J. Am. Chem. Soc. 132 (2010) 15459–61. doi:10.1021/ja104771z.

[5] B.J. Albert, S.H. Pahng, N. Alaniva, E.L. Sesti, P.W. Rand, E.P. Saliba, et al., Instrumentation for cryogenic magic angle spinning dynamic nuclear polarization using 90 L of liquid nitrogen per day, J. Magn. Reson. 283 (2017) 71–78. doi:10.1016/j.jmr.2017.08.014.

[6] K.R. Thurber, R. Tycko, Low-temperature dynamic nuclear polarization with helium-cooled samples and nitrogen-driven magic-angle spinning, J. Magn. Reson. 264 (2016) 99–106. doi:10.1016/j.jmr.2016.01.011.

[7] C. von Morze, J. Tropp, A.P. Chen, I. Marco-Rius, M. Van Criekinge, T.W. Skloss, et al., Sensitivity enhancement for detection of hyperpolarized 13C MRI probes with 1H spin coupling introduced by enzymatic transformation in vivo, Magn. Reson. Med. 41 (2017)

36–41. doi:10.1002/mrm.27000.

[8] D. Lee, E. Bouleau, P. Saint-Bonnet, S. Hediger, G. De Paëpe, Ultra-low temperature MAS-DNP, J. Magn. Reson. 264 (2016) 116–124. doi:10.1016/j.jmr.2015.12.010.

[9] J.H. Ardenkjaer-Larsen, B. Fridlund, A. Gram, G. Hansson, L. Hansson, M.H. Lerche, et al., Increase in signal-to-noise ratio of 10,000 times in liquid-state NMR, Proc. Natl. Acad. Sci. 100 (2003) 10158–10163. doi:10.1073/pnas.1733835100.

[10] A.B. Barnes, M.L. Mak-Jurkauskas, Y. Matsuki, V.S. Bajaj, P.C. a van der Wel, R. DeRocher, et al., Cryogenic sample exchange NMR probe for magic angle spinning dynamic nuclear polarization, J. Magn. Reson. 198 (2009) 261–270. doi:10.1016/j.jmr.2009.03.003.

[11] F.J. Scott, E.P. Saliba, B.J. Albert, N. Alaniva, E.L. Sesti, C. Gao, et al., Frequency-agile gyrotron for electron decoupling and pulsed dynamic nuclear polarization, J. Magn. Reson. 289 (2018) 45–54. doi:10.1016/j.jmr.2018.02.010.

[12] E.P. Saliba, E.L. Sesti, F.J. Scott, B.J. Albert, E.J. Choi, N. Alaniva, et al., Electron Decoupling with Dynamic Nuclear Polarization in Rotating Solids, J. Am. Chem. Soc. 139 (2017) 6310–6313. doi:10.1021/jacs.7b02714.

[13] E.L. Sesti, N. Alaniva, P.W. Rand, E.J. Choi, B.J. Albert, E.P. Saliba, et al., Magic Angle Spinning NMR Below 6 K with a Computational Fluid Dynamics Analysis of Fluid Flow and Temperature Gradients, J. Magn. Reson. (2017). doi:10.1016/j.jmr.2017.11.002.

[14] A.B. Barnes, E. Markhasin, E. Daviso, V.K. Michaelis, E.A. Nanni, S.K. Jawla, et al., Dynamic nuclear polarization at 700MHz/460GHz, J. Magn. Reson. 224 (2012) 1–7.

doi:10.1016/j.jmr.2012.08.002.

[15] P.P. Woskov, V.S. Bajaj, M.K. Hornstein, R.J. Temkin, R.G. Griffin, Corrugated Waveguide and Directional Coupler for CW 250-GHz Gyrotron DNP Experiments, IEEE Trans. Microw. Theory Tech. 53 (2005) 1863–1869.

[16] E.A. Nanni, S.K. Jawla, M.A. Shapiro, P.P. Woskov, R.J. Temkin, Low-loss transmission lines for high-power terahertz radiation, J. Infrared, Millimeter, Terahertz Waves. 33 (2012) 695–714. doi:10.1007/s10762-012-9870-5.

[17] Y. Matsuki, T. Idehara, J. Fukazawa, T. Fujiwara, Advanced instrumentation for DNP-enhanced MAS NMR for higher magnetic fields and lower temperatures, J. Magn. Reson. 264 (2016) 107–115. doi:10.1016/j.jmr.2016.01.022.

[18] E.O. Stejskal, J. Schaefer, J.S. Waugh, Magic-Angle Spinning and Polarization Transfer in Proton-Enhanced NMR, J. Magn. Reson. 28 (1977) 105–12. doi:https://doi.org/10.1016/0022-2364(77)90260-8.

[19] J. Schaefer, R.A. McKay, Multi-Tuned Single Coil Transmission Line Probe for Nuclear Magnetic Resonance Spectrometer, 1999.

[20] R.A. McKay, Probes for Special Purposes, Encycl. Magn. Reson. (2007) 1–4. doi:10.1002/9780470034590.emrstm0416.

[21] M. Rosay, M. Blank, F. Engelke, Instrumentation for solid-state dynamic nuclear polarization with magic angle spinning NMR, J. Magn. Reson. 264 (2016) 88–98. doi:10.1016/j.jmr.2015.12.026.

[22] D.E.M. Hoff, B.J. Albert, E.P. Saliba, F.J. Scott, E.J. Choi, M. Mardini, et al., Frequency swept microwaves for hyperfine decoupling and time domain dynamic nuclear polarization, Solid State Nucl. Magn. Reson. 72 (2015) 79–89. doi:10.1016/j.ssnmr.2015.10.001.

[23] K.J. Pike, T.F. Kemp, H. Takahashi, R. Day, A.P. Howes, E. V. Kryukov, et al., A spectrometer designed for 6.7 and 14.1 T DNP-enhanced solid-state MAS NMR using quasi-optical microwave transmission, J. Magn. Reson. 215 (2011) 1–9. doi:10.1016/j.jmr.2011.12.006.

[24] F.J. Scott, E.L. Sesti, E.J. Choi, A.J. Laut, J.R. Sirigiri, A.B. Barnes, Magic Angle Spinning NMR with Metallized Rotors as Cylindrical Microwave Resonators, (n.d.). doi:10.1002/mrc.4744.

[25] D.D. Traficante, Impedance: What it is, and why it must be matched, Concepts Magn. Reson. Part A1. 1 (1989) 73–92. doi:https://doi.org/10.1002/cmr.1820010205.

[26] Y. Matsuki, S. Nakamura, S. Fukui, H. Suematsu, T. Fujiwara, Closed-cycle cold helium magic-angle spinning for sensitivity-enhanced multi-dimensional solid-state NMR, J. Magn. Reson. 259 (2015) 76–81. doi:10.1016/j.jmr.2015.08.003.

[27] J.A. Stringer, G.P. Drobny, Methods for the analysis and design of a solid state nuclear magnetic resonance probe, Rev. Sci. Instrum. 69 (1998) 3384–3391. doi:10.1063/1.1149104.

[28] H. Yang, D. Staveness, S.M. Ryckbosch, A.D. Axtman, B.A. Loy, A.B. Barnes, et al., REDOR NMR reveals multiple conformers for a protein kinase c ligand in a membrane

environment, ACS Cent. Sci. 4 (2018) 89–96. doi:10.1021/acscentsci.7b00475.

[29] K.A. Collier, S. Sengupta, C.A. Espinosa, J.E. Kelly, J.I. Kelz, R.W. Martin, Design and construction of a quadruple-resonance MAS NMR probe for investigation of extensively deuterated biomolecules, J. Magn. Reson. 285 (2017) 8–17. doi:10.1016/j.jmr.2017.10.002.

Chapter 3:

A Frequency-agile Gyrotron for Frequency-chirped Dynamic Nuclear Polarization with Magic Angle Spinning

Foreword

This chapter is a reproduction of the 2018 Journal of Magnetic Resonance publication, "Frequency-chirped dynamic nuclear polarization with magic angle spinning using a frequency-agile gyrotron" (*Alaniva, N.; *Gao, C.; Saliba, E. P.; Sesti, E. L.; Judge, P. T.; Scott, F. J.; Halbritter, T.; Sigurdsson, S. Th.; Barnes, A. B. (2019) "Frequency-chirped dynamic nuclear polarization with magic angle spinning using a frequency-agile gyrotron". J. Mag. Res. **308**. doi: 10.1016/j.jmr.2019.106586). It is reproduced with the permission of the Journal of Magnetic Resonance. Here, the frequency-agility and high power of the gyrotron are exploited for the demonstration of frequency-chirped dynamic nuclear polarization (DNP). Both frequency-agility and power are useful in the manipulation of the electron-nuclear dipolar interaction. In this chapter, frequency-agility and power are used to increase the effect of DNP, affording even greater signal enhancements. The following chapter will discuss the use of a frequency-agile gyrotron in a rapid-acquisition pulse sequence where the gyrotron must switch between DNP and electron decoupling frequency conditions on a millisecond timescale and perform stably in this switching regime over the course of hours. The range of the microwave frequency output exhibited here is put to use when utilizing different unpaired electron systems for DNP, like ^{14}N-endofullerenes whose DNP condition lies at 197.483 GHz.

3.1 Overview

We demonstrate that frequency-chirped dynamic nuclear polarization (DNP) with magic angle spinning (MAS) improves the enhancement of nuclear magnetic resonance (NMR) signal beyond that of continuous-wave (CW) DNP. Using a custom, frequency-agile gyrotron we implemented frequency-chirped DNP using the TEMTriPol-1 biradical, with MAS NMR at 7 Tesla. Frequency-chirped microwaves yielded a DNP enhancement of 137, an increase of 19% compared to 115 recorded with CW. The chirps were 120 MHz-wide and centered over the trityl resonance, with 7 W microwave power incident on the sample (estimated 0.4 MHz electron spin Rabi frequency). We describe in detail the design and fabrication of the frequency-agile gyrotron used for frequency-chirped MAS DNP. Improvements to the interaction cavity and internal mode converter yielded efficient microwave generation and mode conversion, achieving >10 W output power over a 335 MHz bandwidth with >110 W peak power. Frequency-chirped DNP with MAS is expected to have a significant impact on the future of magnetic resonance

3.2 Introduction

In dynamic nuclear polarization (DNP), the large polarization present in an electron spin reservoir is transferred to nuclear spins, thereby enhancing the intrinsically low sensitivity of nuclear magnetic resonance (NMR) [1–13]. Solid-state NMR and DNP can be combined with magic angle spinning (MAS), which averages anisotropic interactions by rotating the sample about an axis set at 54.7° with respect to the static magnetic field. MAS NMR is a spectroscopic platform that can describe complex molecular and biological architectures [14–20]. Continuous-wave (CW) DNP enhances NMR signal-to-noise by orders of magnitude at moderate magnetic fields and cryogenic sample temperatures. DNP performance is expected to improve at higher magnetic field strengths (14-28 T) and higher temperatures with time-domain DNP [21–24].

Time-domain DNP holds considerable promise to extend MAS DNP to room temperature, at which high-resolution spectra of dynamic molecules can be recorded. MAS DNP experiments are typically performed at cryogenic temperatures (<100 K) due to spin relaxation properties competing with DNP mechanisms. In order to improve performance at high fields and room temperature with time-domain DNP and MAS, a microwave source of sufficient power is required to control electron spins with pulses [21]. Between time-domain DNP and CW DNP lies frequency-chirped DNP, which improves upon CW DNP with modulations in the frequency of the microwave irradiation. Important contributions from Han, Ansermet, Bodenhausen, and colleagues have clearly demonstrated the advantages of modulated, or chirped DNP in static experiments [25–27]. We emphasize that the experiments described in this contribution are not referred to as "time-domain" DNP, as time-domain DNP should be reserved to describe well-characterized coherent electron spin manipulation. Here we describe a variation of the microwave frequency in the time domain, which can be referred to as chirped DNP, or chirped microwaves and its application with MAS.

Gyrotron oscillators are coherent microwave sources well-suited for chirped and time-domain DNP since they can be made frequency-agile, output relatively high power levels, and efficiently scale to higher frequencies [26,28–36]. Current MAS instrumentation prohibits the implementation of a microwave resonator, which is often used in static experiments to generate a high electron Rabi frequency [37,38]. However, with relatively high power output, gyrotrons do not require a sample resonator to achieve the necessary microwave fields for time-domain DNP, thereby enabling frequency-chirped and time-domain DNP with MAS.

Here, we present frequency-chirped DNP with MAS using a coherent, high-power frequency-agile gyrotron. We achieve a 19% gain in enhancement over CW DNP with frequency chirps of

7 W microwave power incident on a sample, which is spun at 4.5 kHz at a temperature of 87 K and a magnetic field of 7 T. The power output of the custom-built 198 GHz frequency-agile gyrotron exceeds 100 W, with a bandwidth of 335 MHz. We describe in detail the design and assembly of this frequency-agile gyrotron used for frequency-chirped DNP in rotating solids. The development of high-power, frequency-agile gyrotrons is expected to drive time-domain MAS DNP toward room temperature and high magnetic fields.

3.3 Methods and Results

3.3.1 Frequency-chirped MAS DNP

The spectra in **Figure 3.1a** show a 19% increase in cross effect DNP enhancement using frequency-chirped microwaves compared to CW irradiation, on a sample of 4 M [U-^{15}N, ^{13}C] urea doped with 5 mM TEMTriPol-1 [39,40]. Microwave frequency chirps over the trityl resonance of TEMTriPol-1 (**Figure 3.2b**) were performed using a frequency-agile gyrotron according to the pulse sequence shown in **Figure 3.1b**. An arbitrary waveform generator (AWG) was used to create voltage waveforms for frequency chirps, which were then amplified 1000× by a high-voltage amplifier (TREK, Inc., Lockport, NY). The amplifier output was electrically connected to the gyrotron anode to control the potential and achieve frequency agility, in the form of frequency-chirped waveforms. The voltage output from the AWG and the high-voltage amplifier are shown in **Figure 3.2a**. Frequency chirps covered a range of 120 MHz and were centered at 197.670 GHz (**Figure 3.2b**). The time for one microwave chirp was 78 μs, with 50 μs up and 28 μs down in frequency. These chirps were repeated over a 20 s DNP period (τ_{pol}, **Figure 3.1b**). The range of the chirps is illustrated by a polychromatic block superimposed on a simulated EPR spectrum of a 1:1 trityl/TEMPO combination. The EPR simulation was generated

with a spin-physics package written in our laboratory, and does not account for interactions between electron spins.

Frequency-chirped microwaves over the resonance condition of the radical have been implemented previously to improve NMR sensitivity through electron decoupling [41,42]. Here, chirped microwaves are applied over the maximum positive cross-effect enhancement condition during the DNP period to increase the DNP enhancements. The DNP period of 20 s utilizes polarization transfer through proton spin diffusion.

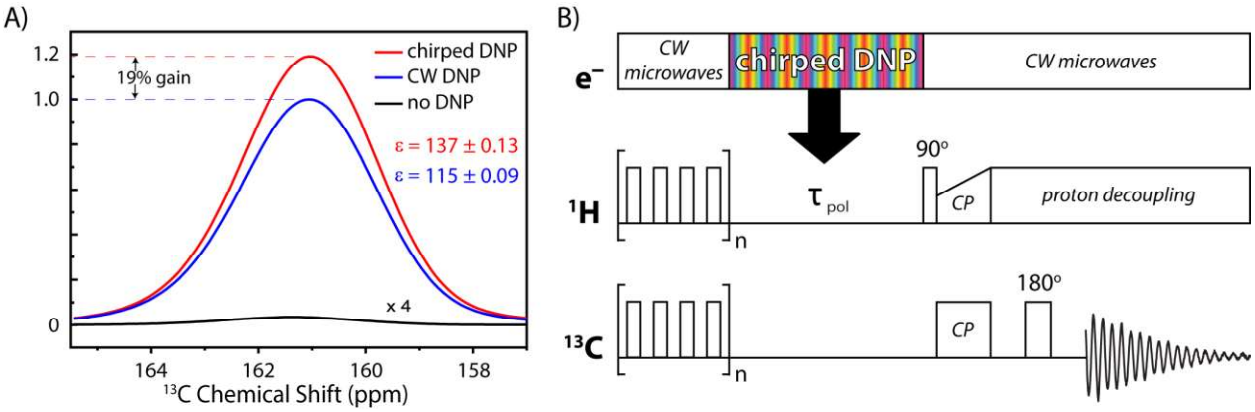

Figure 3.1: a.) *Spectra of 4 M [U-15N, 13C] urea with 5 mM TEMTriPol-1 in d8-glycerol, D2O, and H2O (60%/30%/10% by volume). The black line is NMR signal without microwave irradiation. The blue line is a CW DNP-enhanced spectrum with an enhancement of 115. The red line is a DNP-enhanced spectrum using frequency chirps with an enhancement of 137.* ***b.)*** *The DNP cross-polarization (CP)-MAS sequence with frequency chirps (polychromatic block) used to conduct frequency-chirped DNP. See section 2.2 for further experimental details.*

The frequency-chirped DNP experiments were performed using a custom-built DNP MAS NMR spectrometer. The spectrometer features two unique elements: a frequency-agile gyrotron and a four-channel, cryogenic transmission-line probe, both of which were designed and assembled at Washington University in St. Louis. A Redstone spectrometer console (Tecmag, Inc., Houston, TX) was used in conjunction with TomCo radiofrequency (RF) amplifiers (TomCo, Adelaide, Australia) to provide RF pulses to the transmission line probe for NMR experiments. The AWG

used to generate the voltage waveforms was housed in the Redstone spectrometer as an integrated channel.

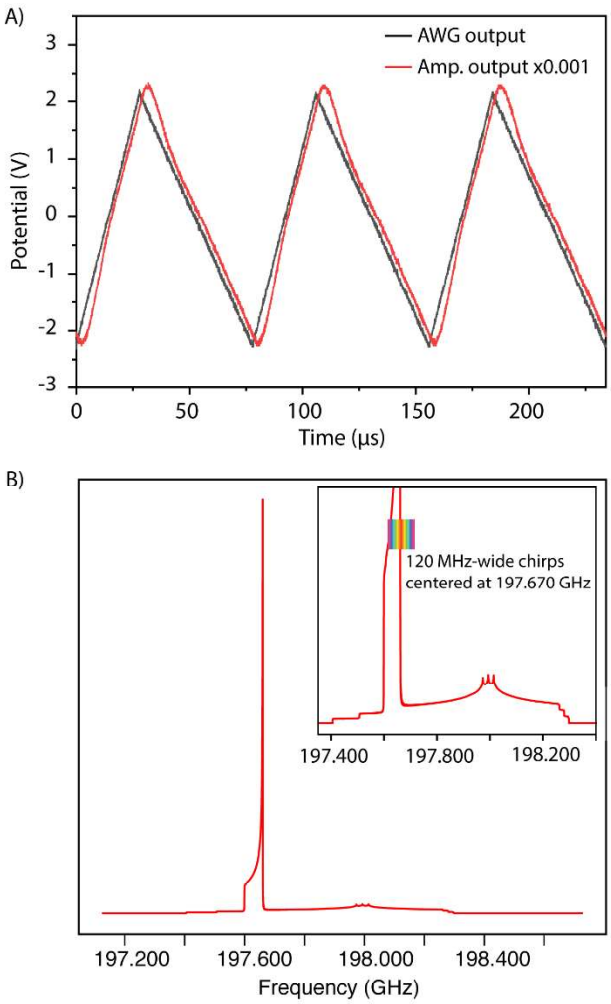

Figure 3.2: a.) *The voltage waveforms used for frequency-chirped DNP. The black trace is the output of the AWG and the red trace is the high-voltage amplifier output, scaled down by a factor of 1000.* ***b.)*** *Simulated EPR spectrum of 1:1 trityl/TEMPO combination. Both the continuous wave irradiation and frequency chirps are centered at 197.670 GHz, the condition for maximum positive cross-effect enhancement [43]. The expansion on the upper-right depicts the range and location of the frequency chirps (polychromatic block) with respect to the EPR spectrum.*

Experiments were performed in a 7.1584 T magnetic field with ^{1}H and ^{13}C Larmor frequencies of 300.1790 MHz and 75.4937 MHz, respectively. The sequence employed ^{1}H-^{13}C cross-polarization MAS (CP-MAS) with a rotor-synchronized Hahn echo (**Figure 3.1a**). A 20 s ($1.26*T_{1DNP}$) DNP transfer period was used during the experiments (**Figure 3.1b**), based on the 15 s DNP buildup time. To remove magnetization buildup, a series of saturation pulses were applied to both the ^{1}H and the ^{13}C spins before the DNP period. CW microwaves of 197.670 GHz irradiated the sample during the saturation, CP, spin-echo, and signal acquisition periods (**Figure 3.1b**). The ^{13}C γB_1 was 33 kHz, and the ^{1}H γB_1 was ramped over the Hartmann-Hahn matching condition to conduct efficient CP. The ^{1}H γB_1 was 83 kHz for the excitation pulse and two pulse phase modulation (TPPM) decoupling [44].

The sample, 4 M [U-^{13}C, ^{15}N] urea with 5 mM TEMTriPol-1 in a cryoprotecting matrix of d_8-glycerol, D_2O, and H_2O (60%/30%/10% by volume), was spun at 4.5 kHz at 87 K for all experiments (a <1 K increase in sample temperature is observed with microwaves on the sample, as determined with KBr T_1 measurements [45]). The temperature was monitored by a calibrated temperature sensor. The TEMTriPol-1 biradical contains a Finland trityl and a 4-amino-TEMPO tethered through a glycine linker. 4-amino-TEMPO is a nitroxide monoradical with a broad electron paramagnetic resonance (EPR) lineshape (~900 MHz), whereas Finland trityl is a stable organic monoradical with a relatively narrow EPR lineshape (~60 MHz). With an EPR profile (**Figure 3.2B**) width that exceeds the ^{1}H Larmor frequency, TEMTriPol-1 utilizes the cross effect DNP mechanism. The microwaves from frequency-agile gyrotron were attenuated to provide an incident power of 7 W and an estimated electron Rabi frequency of 0.4 MHz on the sample. 7 W was used as the optimized power to yield the highest DNP enhancement. The microwave power was attenuated with an adjustable copper-slit apparatus that allowed a variable amount of microwave power to pass to the sample. Incident microwave power was calculated using water-load power measurements and previously-determined attenuation of the reduced-diameter waveguide that interfaces with the NMR MAS probe head. The beam current was maintained at 183 mA, varying by less than 3 mA during microwave chirping. The gyrotron operating parameters are summarized in **Table 3.1**.

Table 3.1: Gyrotron operating parameters.

Operating mode $TE_{m,n,q}$	$TE_{5,2,q}$
Frequency	197.570-197.905 GHz
Voltage tuning range	335 MHz
Cavity magnetic field B	7.16 T
Cyclotron harmonic	1st
Beam voltage V_b	9-14 kV
Beam current I_b	183 mA
Output power	up to 112W
Compression factor	29

3.3.2 Gyrotron Power Output

The gyrotron achieved a peak power of 112 W, and a frequency bandwidth of 335 MHz with power >10 W (**Figure 3.3**). The microwave power was measured with a calorimeter (Scientech, Inc., Boulder, CO), which was calibrated at multiple operation parameters using a water load. The frequency was detected with a frequency measurement system (Bridge 12 Technologies, Inc., Framingham, MA). All experiments were conducted with a beam current of 183 mA. The gyrotron achieved an output efficiency of 4.4% with 112 W power output at 14 kV beam potential (V_b) and 183 mA beam current (I_b).

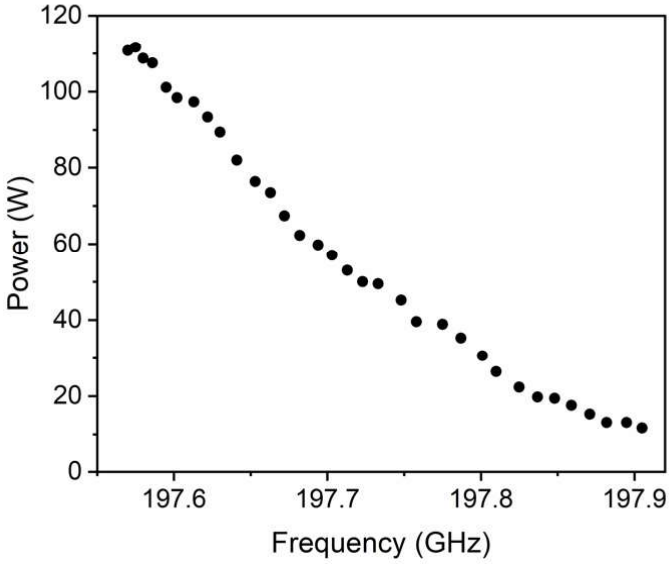

Figure 3.3*: Power and bandwidth of the 198 GHz gyrotron. The microwave power shown was measured at the gyrotron window. A power output of >10 W is available over 335 MHz bandwidth, with a peak power of 112 W.*

We note that the commercially available 263 GHz CW gyrotrons manufactured by CPI (Communications & Power Industry) for Bruker Biospin DNP spectrometers, operating at TE_{03} mode, can output 75 W microwave power at slightly higher efficiency (~10%) with a 15 kV and 50 mA electron beam [36,46]. However, the microwave tuning range in this comparable commercial gyrotron is 100 MHz and there is currently no capability for fast frequency modulation.

3.4 Gyrotron Design

In a gyrotron, electrons are thermionically emitted from a barium-impregnated tungsten ring when the cathode is heated by an alternating current. A potential between the cathode and anode accelerates the electron beam, whose radius is compressed as it propagates through the magnetic field. The electron beam reaches a maximum compression in the interaction cavity, where a

combination of electron cyclotron motion and phase bunching converts kinetic energy into microwave energy. This gyrotron generates microwaves in the $TE_{5,2,q}$ mode. Acceleration of electron beam partially determines the electron cyclotron frequency, and therefore the frequency of the microwaves generated. The spent electron beam exits the cavity and propagates to the water-cooled copper collector. Microwaves propagate through the internal mode converter where they are converted to a Gaussian-like mode before being directed out of the gyrotron tube through a sapphire window.

This gyrotron utilizes a ceramic break (**Figure 3.4**) to electrically isolate the anode such that the potential can be controlled by high-voltage waveforms to achieve microwave frequency agility. We have used previous gyrotrons to develop novel techniques such as electron decoupling [41–43]. Here we describe the design and construction of a gyrotron with improved power output for frequency-chirped DNP. Major design improvements were made in three main areas: the magnetron injection gun (MIG), the interaction cavity, and the internal mode converter (**Figure 3.4**).

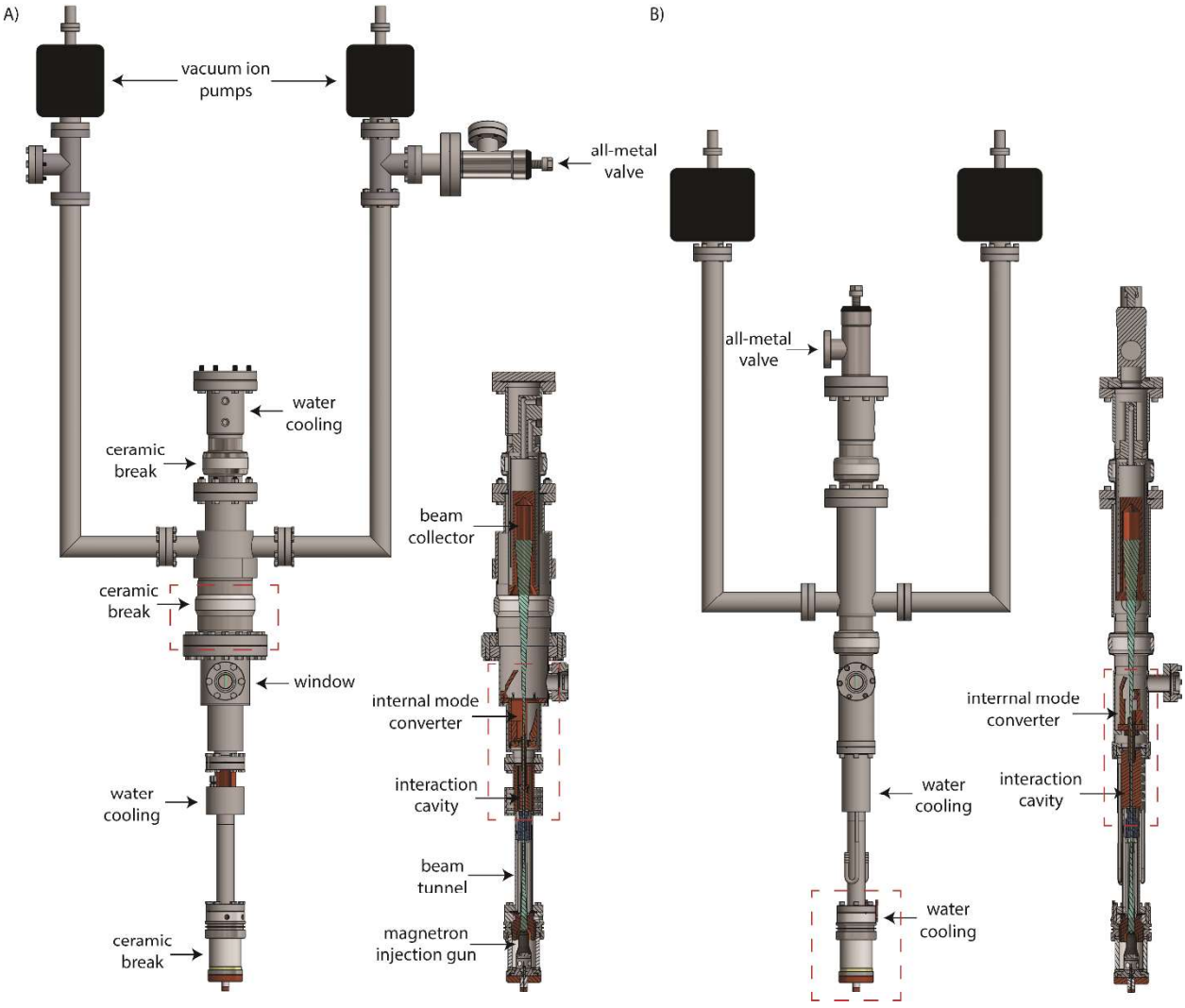

Figure 3.4: *Schematics of frequency-agile gyrotrons.* ***A)*** *Full view and cross section of the improved gyrotron for frequency-chirped DNP experiments.* ***B)*** *Full view and cross section of the gyrotron described by Scott et al. [43]. Red dashed boxes indicate areas that are shown in later figures with more detail.*

3.4.1 Magnetron Injection Gun (MIG)

The MIG provides a reservoir of electrons and the necessary geometry for electron beam generation. **Figure 3.5** illustrates the MIG design of a gyrotron described by Scott et al. (will be referred to as "Scott et al. gyrotron"), which utilized an in-body water cooling system to maintain ambient operating temperature for the MIG [43]. The proximity of the brass connection to the grounded gyrotron magnet bore resulted in several arcing events when the potential was modulated for frequency chirps. In the improved design these brass connections were removed

and external air cooling was used instead, maximizing the space between the MIG and the magnet bore to avoid arcing events.

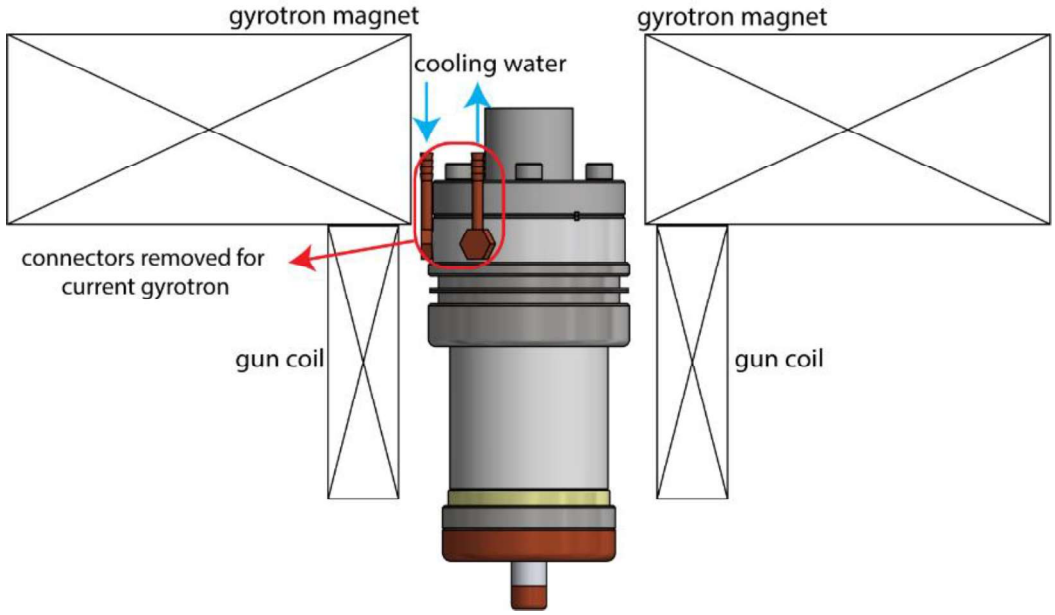

***Figure 3.5**: Schematic of the MIG with brass connectors to water cooling lines in Scott et al. gyrotron [43]. These connectors were removed in the current gyrotron.*

3.4.2 Interaction Cavity

The alignment of the cylindrical interaction cavity and the precision of its radius are paramount for obtaining high-power microwave output at the intended frequency and mode. Tapered sections on either side of the interaction cavity prevent undesired microwave modes (parasitic oscillations) (**Figure 3.7**). To facilitate precise fabrication of the interaction cavity, this gyrotron design features an interaction cavity body separate from the tapered segments. The interaction cavity was attached to the up-taper using set screws with pins to ensure proper alignment. While the Scott et al. gyrotron featured a 30 mm-long interaction cavity (**Figure 3.7b** and red box of cross section in **Figure 3.4B**), this gyrotron was designed with a cavity length of 25 mm (**Figure 3.6, 3.7a** and the red box of cross section in **Figure 3.4a**) [43]. Note, the 25 mm length is

roughly 17 wavelengths (198 GHz), and is sufficient to lead to the excitation of hybridized axial modes in the cavity and continuous frequency tuning, as has been observed previously [31,47].

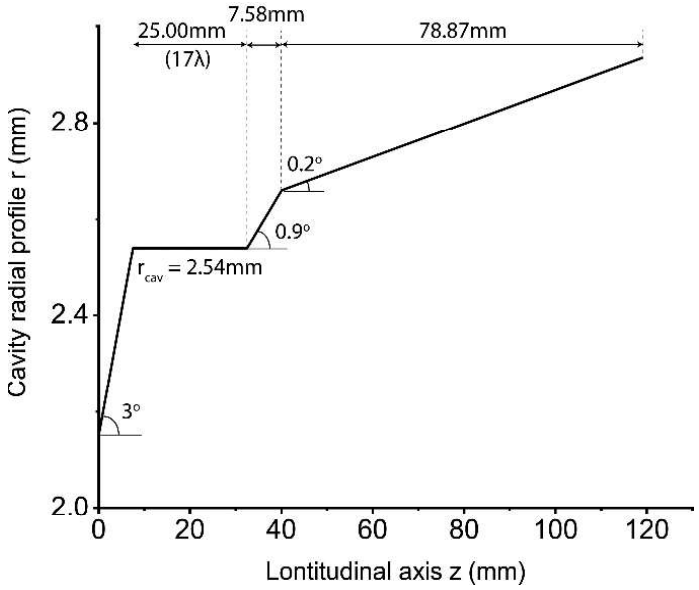

Figure 3.6: *Geometry of the interaction cavity and up-taper in the current 198 GHz gyrotron. The interaction cavity contains a down-taper and a 25 mm straight section. The 86 mm up-taper is machined as a separate piece.*

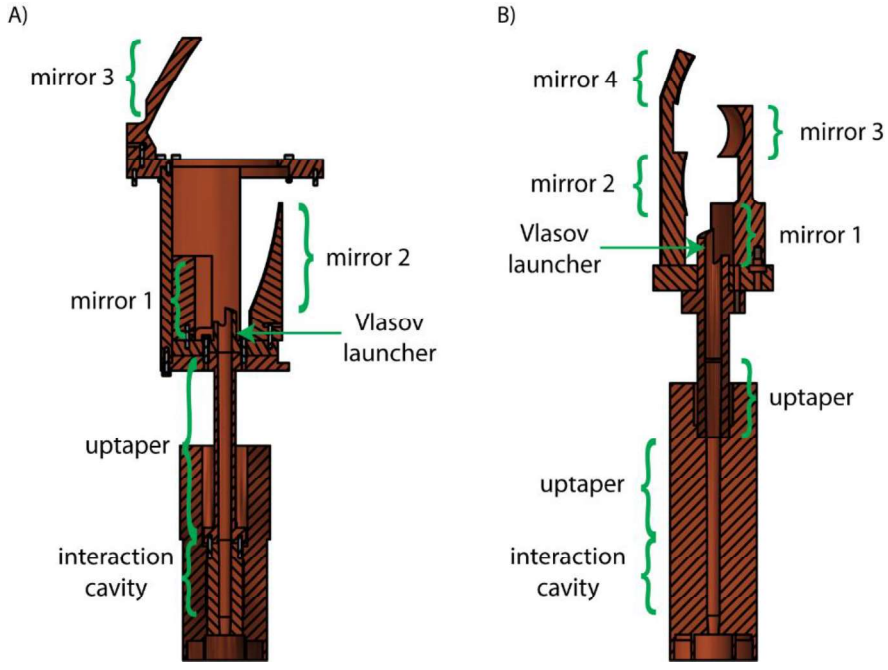

Figure 3.7*: Section views of internal mode converter and interaction cavity assembly of* ***a.)*** *the current gyrotron and* ***b.)*** *the Scott et al. gyrotron [43].*

3.4.3 Internal Mode Converter

The $TE_{5,2,q}$ mode microwaves generated in the interaction cavity travel up and are directed toward a series of parabolic mirrors by the helical cut of the Vlasov launcher (**Figure 3.7a,b**). The $TE_{5,2,q}$ is a rotating mode, so the Vlasov launcher needs to be helically cut to optimize mode conversion (**Figure 3.8b**). The series of concave mirrors continue to shape the microwave beam profile until the microwaves are directed out of gyrotron through the sapphire window [43,47]. The resulting microwave beam with Gaussian-like mode couples efficiently to the $HE_{1,1}$ mode supported by the corrugated, overmoded waveguide [48].

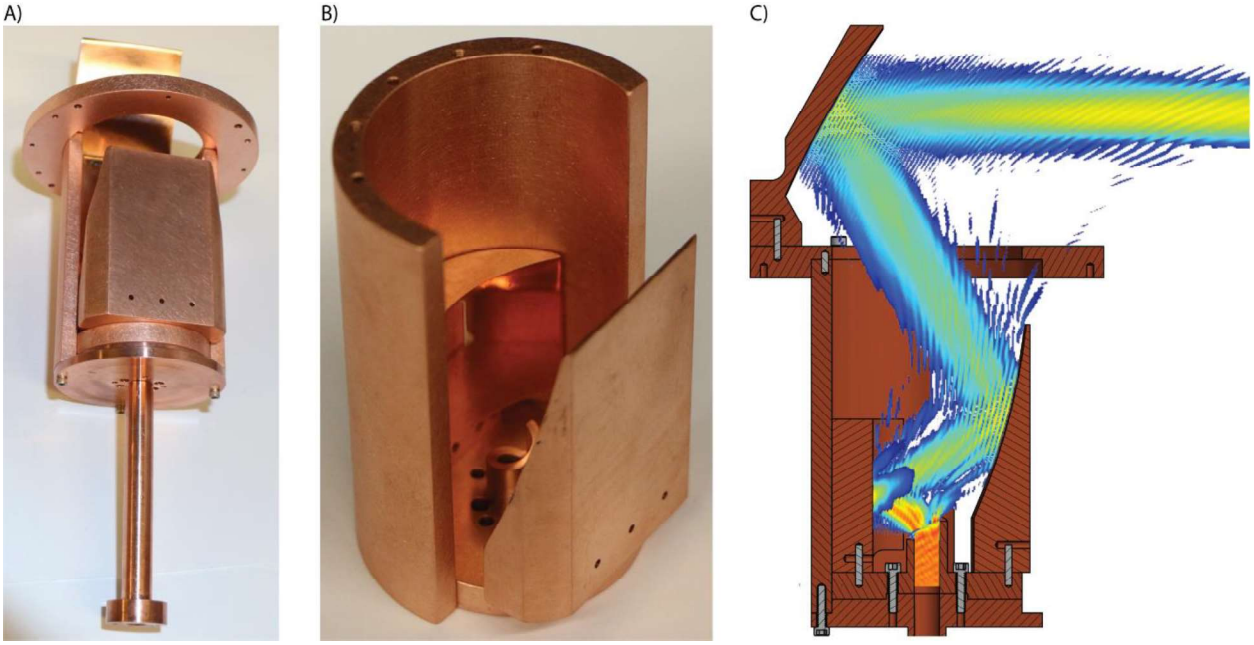

***Figure 3.8**: Internal mode converter of the current gyrotron. **a.)** Photograph of the internal mode converter assembly. **b.)** Photograph of the lower two mirrors and the helical Vlasov launcher. **c.)** Section view of microwave intensity simulation in the internal mode converter. Microwave intensity plots were calculated by Bridge 12 Technologies, Inc.*

Microwave power is lost when reflected by mirrors with slight misalignment, so reducing the number of mirrors reduces the possibility of misalignment and increases power output. The current gyrotron uses two concave mirrors rather than three described previously by Scott et al. (**Figure 3.7a and 3.8**) [43]. The orientation and location of the mirrors were optimized for

microwave mode conversion, with stainless steel dowel pins for proper alignment. Mirror surface geometry and alignment were optimized by Bridge12 Technologies, Inc. (Framingham, MA) using an electromagnetics simulation program (**Figure 3.8c**). The supporting structures were then designed in Autodesk Inventor (Autodesk Inc., San Rafael, CA) to align the mirrors and properly direct microwaves out of the gyrotron window. Copper mirrors were fabricated on a computer numerical control milling machine by Ramco Machine (Rowley, MA).

Since microwaves are not directed out of the window with 100% efficiency, stray microwaves are absorbed by the gyrotron body. The temperature of the ceramic break above the window (red box of full view in **Figure 3.4a**) rises as the ceramic-break region absorbs microwaves improperly reflected by the internal mode converter. This can be an effect of misaligned mirrors and/or the generation of non-$TE_{5,2,q}$ mode microwaves. The improvements made to interaction cavity and internal mode converter led to more efficient microwave generation and $TE_{5,2,q}$-Gaussian mode conversion, which contribute to the maximum microwave power output of 112 W.

3.4.4 Gyrotron Construction

Gyrotron construction requires purchasing of commercial parts as well as incorporating them with custom-designed and custom-built parts. Most gyrotron parts were machined in the Washington University Chemistry Department machine shop, with welding conducted at Laciny Bros., Inc. (University City, MO). The brazing required for stainless steel and copper connection was done by Ceramic-To-Metal Seals, Inc. (Winchester, MA). Ceramic breaks and CF flanges were provided by MDC Vacuum Products LLC. (Hayward, CA). Vacuum ion pumps were purchased from Duniway Stockroom Corp. (Fremont, CA). The 7 T cryogen-free gyrotron magnet was custom-developed by Cryomagnetics, Inc. (Oak Ridge, TN) and is used, in

conjunction with the gyrotron, to generate microwave irradiation for all DNP experiments. The superconducting gyrotron magnet has an inner bore diameter of 83.8 mm. The cavity is positioned at the magnet center, where the magnetic field is 7.16 T. The emitter is located 238 mm lower than the cavity, where the superconducting magnetic field is 3.36 T. A smaller, resistive "gun coil" magnet is installed below the superconducting magnet (at the MIG, **Figure 3.5**) for fine adjustment of the gyrotron operation.

An ultra-high vacuum ($\leq 10^{-8}$ Torr) inside the gyrotron is imperative for optimal performance. Oxygen and water molecules can react with the cathode emitter at high temperatures, resulting in an increased work function and sub-optimal electron emission. Also, remaining gas present between cathode and anode, which are under high potential during operation, could become ionized and cause arcing. These important aspects of gyrotron operation require careful attention in construction to achieve the ultra-high vacuum.

A water-based detergent was first used to remove visible greases from machining, followed by acetone to remove detergent and water from stainless-steel surfaces. Ethanol was then used to remove remaining acetone and water due to its higher volatility. Copper parts, such as the internal mode converter and interaction cavity, were cleaned by sonication in ethanol for 30 minutes because of their delicate features and geometry. Lint-free wipes were used during cleaning to avoid fibers on the inner surface of gyrotron parts.

After cleaning, a helium leak detector (Pfeiffer Vacuum, Nashua, NH) was used to examine all welding joints on each gyrotron part, as well as flange connections. The gyrotron parts, except for the MIG, were assembled for the first bakeout. This is to avoid contamination of the MIG cathode (**Figure 3.9a**) in the case of unforeseen failures of joints, which can lead to high pressure

events during bakeout. All bolts used for assembly were lightly coated with Loctite metal-free lubricant to avoid seizing after thermocycles. A custom-built support kept the gyrotron in place during the assembly and bakeout (**Figure 3.9**).

Figure 3.9*: Gyrotron bakeout.* ***a.)*** *Assembled gyrotron connecting to a turbomolecular pump.* ***b.)*** *Gyrotron wrapped with heating tapes. Thermocouples are placed in different regions to monitor temperatures.* ***c.)*** *The gyrotron is further wrapped in aluminum foil to trap heat.*

A nitrogen backfill was conducted to further remove any contaminants adsorbed onto the inner surface of gyrotron. According to Le Châtelier's principle, and the 2nd law of Thermodynamics, molecules adsorbed onto the surface will enter the gaseous phase when the partial pressure of that molecule decreases, until a new equilibrium is reached. The pressure of backfilling nitrogen inside the gyrotron was kept below 2 atm to prevent damage on the sapphire window.

During the bakeout, the gyrotron was heated by heating tape while the turbomolecular pump was pulling a vacuum. The heating tape was controlled by variable AC transformers (VARIAC Inc., Cleveland, OH), and monitored by thermocouples (**Figure 3.9b**). After a uniform temperature was achieved over the gyrotron, aluminum foil was wrapped around the gyrotron for insulation (**Figure 3.9c**). The gyrotron body was heated to 250°C, and the collector to a higher temperature (300°C) due to its high outgassing possibility when the spent electron beam reaches the inner surface. The bolts were tightened again at the maximum temperature due to the different

expansion of copper gaskets and stainless steel. When the turbomolecular pump reported a stable pressure, the ion pumps were turned on to further pull a high vacuum. The gyrotron was slowly cooled back to room temperature once the desired pressure, $\leq 10^{-8}$ Torr, was achieved. The turbomolecular pump was connected to the arm of the gyrotron rather than to the top of the collector for Scott et al. gyrotron (**Figure 3.4Aa,b**) [43], allowing a maximized cross-sectional area of the vacuum path to improve conductance.

MIG activation involves heating the cathode with an alternating current and applying a low potential to obtain electron emission. **Figure 3.10a,c** shows the setup for MIG activation, during which the vacuum inside MIG was maintained below 10^{-8} Torr. A circuit diagram of MIG activation is shown in **Figure 3.10b**.

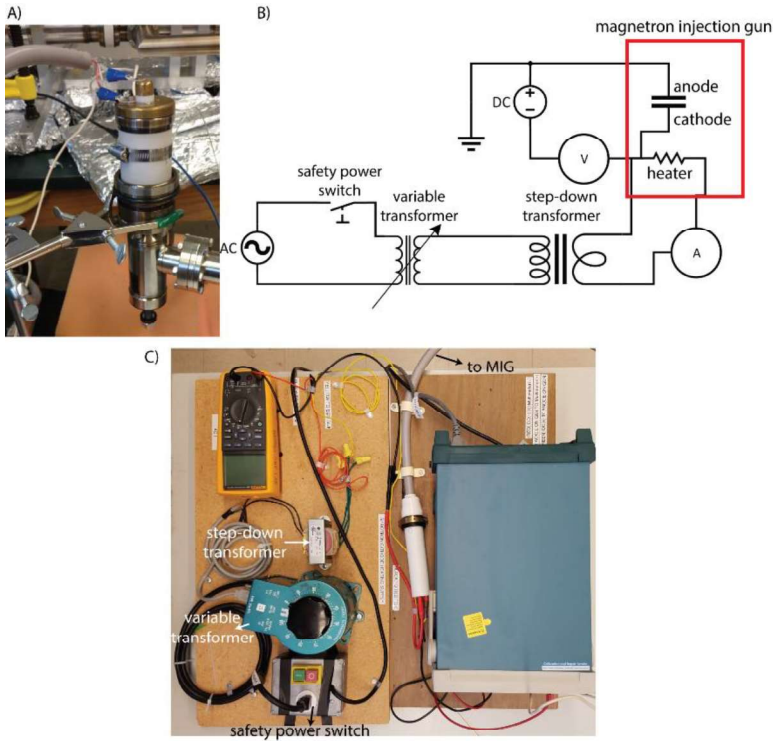

***Figure 3.10**: MIG activation. **a.)** Photograph of MIG during activation. b.) Circuit diagram of the AC and DC circuits during MIG activation. c.) Photograph of the circuit diagram.*

The AC current was regulated by a variable transformer with a step-down converter to reduce the maximum potential. The DC potential was supplied by a Tektronix power supply (Beaverton, OR), with emission current detected by a Tektronix multimeter. The MIG was kept at a low DC potential while the cathode was hot (AC ~ 2.0 A), until an increasing emission was observed. Then the potential was slowly increased and stayed at ~15 V until the first stage of the bakeout was completed.

All copper gaskets and bolts on the gyrotron were replaced following the first bakeout, since the copper can be deformed after compression and bolts can weaken with thermocycling. In order to avoid contamination, a nitrogen backfill was implemented during the gyrotron reassembly. The second bakeout procedure was the same as the first, except the activated MIG was attached to the vacuum tube. Heated by its internal heater with ~2.0 A alternating current, the MIG needs no heating tape on the outside. When the desired vacuum was achieved, other parts of the gyrotron were cooled gradually before the AC power in the MIG was reduced, in order to avoid gas adsorption into the porous barium-tungsten emitter.

3.5 Conclusion and Outlook

Frequency-chirped DNP MAS achieves 19% greater DNP enhancement compared to CW irradiation, using the frequency-agile gyrotron presented here. Improvements in the interaction cavity and internal mode convertor of the gyrotron resulted in efficient microwave generation and mode conversion, thus achieving a ~3-fold gain in microwave power output compared to a previously reported gyrotron [43].

The development of a MAS microwave resonator [49] with a high quality factor would further increase electron Rabi frequencies and better manipulate electron spins. Moreover, frequency-

chirped DNP MAS can be optimized in terms of the voltage waveform, rotor rotation frequency, and the type and concentration of the doped radicals. Although the microwave output was frequency-chirped, the sample was still exposed to constant high-power microwave irradiation, restraining the experimental temperatures to < 100 K. However, by controlling the anode potential to terminate microwave power, frequency chirps could be performed in a way that limits the duty cycle. These methodological improvements will be necessary to perform frequency-chirped and time-domain DNP MAS at room temperature and high magnetic fields.

3.5 Acknowledgements

Funding: This research was supported by a NIH Director's New Innovator Award [grant number DP2GM119131], an NSF CAREER Award [grant number DBI-1553577], a Camille Dreyfus teacher-scholar award, and the Deutsche Forschungsgemeinschaft (DFG) postdoc fellowship (414196920), and the University of Iceland Research Fund.

References

[1] A.W. Overhauser, Polarization of Nuclei in Metals, Phys. Rev. 92 (1953) 411–415.

[2] T.R. Carver, C.P. Slichter, Polarization of nuclear spins in metals, Phys. Rev. 92 (1953) 212–213. doi:10.1103/PhysRev.92.212.2.

[3] T. Kobayashi, A. Perras, I.I. Slowing, A.D. Sadow, M. Pruski, Dynamic Nuclear Polarization Solid-State NMR in Heterogeneous Catalysis Research, ACS Catal. 5 (2015) 7055–7062. doi:10.1021/acscatal.5b02039.

[4] D. Yoon, M. Soundararajan, C. Caspers, F. Braunmueller, J. Genoud, S. Alberti, J. Ansermet, 500-fold enhancement of in situ 13 C liquid state NMR using gyrotron-driven

temperature-jump DNP, J. Magn. Reson. 270 (2016) 142–146. doi:10.1016/j.jmr.2016.07.014.

[5] A.S. Lilly Thankamony, J.J. Wittmann, M. Kaushik, B. Corzilius, Dynamic nuclear polarization for sensitivity enhancement in modern solid-state NMR, Prog. Nucl. Magn. Reson. Spectrosc. 102–103 (2017) 120–195. doi:10.1016/j.pnmrs.2017.06.002.

[6] M. Afeworki, J. Schaefer, Mechanism of DNP-Enhanced Polarization Transfer across the Interface of Polycarbonate/Polystyrene Heterogeneous Blends, Macromolecules. 25 (1992) 4092–4096. doi:10.1021/ma00042a007.

[7] M. Afeworki, S. Vega, J. Schaefer, Direct Electron-to-Carbon Polarization Transfer in Homogeneously Doped Polycarbonates, Macromolecules. 25 (1992) 4100–4105. doi:10.1021/ma00042a009.

[8] M.J. Duijvestijn, C. van der Lugt, J. Smidt, R.A. Wind, K.W. Zilm, D.C. Staplin, 13C NMR spectroscopy in diamonds using dynamic nuclear polarization, Chem. Phys. Lett. 102 (1983) 25–28. doi:10.1016/0009-2614(83)80650-2.

[9] M.J. Duijvestijn, A. Manenschijn, J. Smidt, R.A. Wind, Structural information of undoped trans-polyacetylene obtained by 13C 2D NMR combined with dynamic nuclear polarization, J. Magn. Reson. 64 (1985) 461–469. doi:10.1016/0022-2364(85)90109-X.

[10] M. Nechtschein, F. Devreux, R.L. Greene, T.C. Clarke, G.B. Street, One-dimensional spin diffusion in polyacetylene, (CH)x, Phys. Rev. Lett. 44 (1980) 356–359. doi:10.1103/PhysRevLett.44.356.

[11] M. Nechtschein, F. Devreux, F. Genoud, M. Guglielmi, K. Holczer, Magnetic-resonance

studies in undoped trans-polyacetylene (CH)x. II, Phys. Rev. B. 27 (1983) 61–78. doi:10.1103/PhysRevB.27.61.

[12] L.R. Becerra, G.J. Gerfen, R.J. Temkin, D.J. Singel, R.G. Griffin, Dynamic nuclear polarization with a cyclotron resonance maser at 5 T, Phys. Rev. Lett. 71 (1993) 3561–3564. doi:10.1103/PhysRevLett.71.3561.

[13] K.-N. Hu, H. Yu, T.M. Swager, R.G. Griffin, Dynamic Nuclear Polarization with Biradicals, J. Am. Chem. Soc. 126 (2004) 10844–10845. doi:10.1021/ja039749a.

[14] V.S. Bajaj, M.L. Mak-Jurkauskas, M. Belenky, J. Herzfeld, R.G. Griffin, Functional and shunt states of bacteriorhodopsin resolved by 250 GHz dynamic nuclear polarization-enhanced solid-state NMR, Proc. Natl. Acad. Sci. 106 (2009) 9244–9249. doi:10.1073/pnas.0900908106.

[15] X. Kang, A. Kirui, A. Muszyński, M.C.D. Widanage, A. Chen, P. Azadi, P. Wang, F. Mentink-Vigier, T. Wang, Molecular architecture of fungal cell walls revealed by solid-state NMR, Nat. Commun. 9 (2018) 1–12. doi:10.1038/s41467-018-05199-0.

[16] X. Kang, A. Kirui, M.C. Dickwella Widanage, F. Mentink-Vigier, D.J. Cosgrove, T. Wang, Lignin-polysaccharide interactions in plant secondary cell walls revealed by solid-state NMR, Nat. Commun. 10 (2019) 1–9. doi:10.1038/s41467-018-08252-0.

[17] R.W. Martin, R.C. Jachmann, D. Sakellariou, U.G. Nielsen, A. Pines, High-Resolution Nuclear Magnetic Resonance Spectroscopy of Biological Tissues Using Projected Angle Spinning, Magn. Reson. Med. 257 (2005) 253–257. doi:10.1002/mrm.20585.

[18] A.N. Smith, U.T. Twahir, T. Dubroca, G.E. Fanucci, J.R. Long, N. High, M. Field, E.P.

Dirac, U. States, Molecular Rationale for Improved Dynamic Nuclear Polarization of Biomembranes, J. Phys. Chem. B. 120 (2016) 7880–7888. doi:10.1021/acs.jpcb.6b02885.

[19] W. Tang, A. Bhatt, A.N. Smith, P.J. Crowley, L.J. Brady, J.R. Long, Specific binding of a naturally occurring amyloidogenic fragment of Streptococcus mutans adhesin P1 to intact P1 on the cell surface characterized by solid state NMR spectroscopy, J. Biomol. NMR. 64 (2016) 153–164. doi:10.1007/s10858-016-0017-1.

[20] D. Daube, M. Vogel, B. Suess, B. Corzilius, Dynamic nuclear polarization on a hybridized hammerhead ribozyme : An explorative study of RNA folding and direct DNP with a paramagnetic metal ion cofactor, Solid State Nucl. Magn. Reson. 101 (2019) 21–30. doi:10.1016/j.ssnmr.2019.04.005.

[21] T. V. Can, J.J. Walish, T.M. Swager, R.G. Griffin, Time domain DNP with the NOVEL sequence, J. Chem. Phys. 143 (2015) 1–8. doi:10.1063/1.4927087.

[22] A. Henstra, P. Dirksen, W.T. Wenckebach, Enhanced dynamic nuclear polarization by the integrated solid effect, Phys. Lett. A. 134 (1988) 134–136. doi:10.1016/0375-9601(88)90950-4.

[23] T. V. Can, R.T. Weber, J.J. Walish, T.M. Swager, R.G. Griffin, Frequency-Swept Integrated Solid Effect, Angew. Chemie - Int. Ed. 56 (2017) 6744–6748. doi:10.1002/anie.201700032.

[24] A. Henstra, P. Ducksen, J. Schmidt, K. Onnes, H. Laboratories, Nuclear Spin Orientation via Electron Spin Locking (NOVEL), J. Magn. Reson. 393 (1988) 389–393.

[25] I. Kaminker, S. Han, Amplification of Dynamic Nuclear Polarization at 200 GHz by

Arbitrary Pulse Shaping of the Electron Spin Saturation Profile, J. Phys. Chem. Lett. 9 (2018) 3110–3115. doi:10.1021/acs.jpclett.8b01413.

[26] D. Yoon, M. Soundararajan, P. Cuanillon, F. Braunmueller, S. Alberti, J.P. Ansermet, Dynamic nuclear polarization by frequency modulation of a tunable gyrotron of 260 GHz, J. Magn. Reson. 262 (2016) 62–67. doi:10.1016/j.jmr.2015.11.008.

[27] A. Bornet, A. Pinon, A. Jhajharia, M. Baudin, X. Ji, L. Emsley, G. Bodenhausen, J.H. Ardenkjaer-Larsende, S. Jannin, Microwave-gated dynamic nuclear polarization †, Phys. Chem. Chem. Phys. (2016) 30530–30535. doi:10.1039/c6cp05587g.

[28] S. Alberti, J.P. Ansermet, K.A. Avramides, D. Fasel, J.P. Hogge, S. Kern, C. Lievin, Y. Liu, A. Macor, I. Pagonakis, M. Silva, M.Q. Tran, T.M. Tran, D. Wagner, Design of a frequency-tunable gyrotron for DNP-enhanced NMR spectroscopy, 34th Int. Conf. Infrared, Millimeter, Terahertz Waves, IRMMW-THz 2009. (2009) 1–2. doi:10.1109/ICIMW.2009.5324906.

[29] V. Vitzthum, M.A. Caporini, G. Bodenhausen, Solid-state nitrogen-14 nuclear magnetic resonance enhanced by dynamic nuclear polarization using a gyrotron, J. Magn. Reson. 205 (2010) 177–179. doi:10.1016/j.jmr.2010.04.014.

[30] M.Y. Glyavin, A. V. Chirkov, G.G. Denisov, A.P. Fokin, V. V. Kholoptsev, A.N. Kuftin, A.G. Luchinin, G.Y. Golubyatnikov, V.I. Malygin, M. V. Morozkin, V.N. Manuilov, M.D. Proyavin, A.S. Sedov, E. V. Sokolov, E.M. Tai, A.I. Tsvetkov, V.E. Zapevalov, Experimental tests of a 263 GHz gyrotron for spectroscopic applications and diagnostics of various media, Rev. Sci. Instrum. 86 (2015) 1–4. doi:10.1063/1.4921322.

[31] A.C. Torrezan, S.T. Han, I. Mastovsky, M.A. Shapiro, J.R. Sirigiri, R.J. Temkin, A.B. Barnes, R.G. Griffin, Continuous-wave operation of a frequency-tunable 460-GHz second-harmonic gyrotron for enhanced nuclear magnetic resonance, IEEE Trans. Plasma Sci. 38 (2010) 1150–1159. doi:10.1109/TPS.2010.2046617.

[32] S. Alberti, F. Braunmueller, T.M. Tran, J. Genoud, J. Hogge, M.Q. Tran, J. Ansermet, Nanosecond Pulses in a THz Gyrotron Oscillator Operating in a Mode-Locked Self-Consistent Q -Switch Regime, Phys. Rev. Lett. 205101 (2013) 1–5. doi:10.1103/PhysRevLett.111.205101.

[33] Y. Matsuki, H. Takahashi, K. Ueda, T. Idehara, I. Ogawa, M. Toda, H. Akutsu, T. Fujiwara, Dynamic nuclear polarization experiments at 14.1 T for solid-state NMR, Phys. Chem. Chem. Phys. 12 (2010) 5799–5803.

[34] Y. Matsuki, T. Idehara, J. Fukazawa, T. Fujiwara, Advanced instrumentation for DNP-enhanced MAS NMR for higher magnetic fields and lower temperatures, J. Magn. Reson. 264 (2016) 107–115. doi:10.1016/j.jmr.2016.01.022.

[35] K. Ueda, Y. Matsuki, T. Fujiwara, Y. Tatematsu, I. Ogawa, T. Idehara, Further Characterization of 394-GHz Gyrotron FU CW GII with Additional PID Control System for 600-MHz DNP-SSNMR Spectroscopy, J. Infrared, Millimeter, Terahertz Waves. (2016) 825–836. doi:10.1007/s10762-016-0276-7.

[36] M. Blank, P. Borchard, S. Cauffman, K. Felch, M. Rosay, L. Tometich, High-Frequency CW Gyrotrons for NMR / DNP Applications, IVEC 2012. (2012) 327–328. doi:10.1109/IVEC.2012.6262182.

[37] D.J. Singel, H. Seidel, R.D. Kendrick, C.S. Yannoni, A spectrometer for EPR, DNP, and multinuclear high-resolution NMR, J. Magn. Reson. 81 (1989) 145–161. doi:10.1016/0022-2364(89)90273-4.

[38] R.A. Wind, R.A. Hall, A. Jurkiewicz, H. Lock, G.E. Maciel, Two Novel DNP-NMR Probes, J. Magn. Reson. Ser. A. 110 (1994) 33–37. doi:10.1006/jmra.1994.1177.

[39] G. Mathies, M.A. Caporini, V.K. Michaelis, Y. Liu, K. Hu, D. Mance, J.L. Zweier, M. Rosay, M. Baldus, R.G. Griffin, Efficient Dynamic Nuclear Polarization at 800 MHz / 527 GHz with Trityl-Nitroxide Biradicals, Angew. Chem - Int. Ed. 54 (2015) 11770–11774. doi:10.1002/anie.201504292.

[40] Y. Liu, F.A. Villamena, J.L. Zweier, Trityl-nitroxide biradicals as unique molecular probes for the simultaneous measurement of redox status and oxygenation, Chem. Commun. 1 (2010) 628–630. doi:10.1039/b919279d.

[41] E.P. Saliba, E.L. Sesti, F.J. Scott, B.J. Albert, E.J. Choi, N. Alaniva, C. Gao, A.B. Barnes, Electron Decoupling with Dynamic Nuclear Polarization in Rotating Solids, J. Am. Chem. Soc. 139 (2017) 6310–6313. doi:10.1021/jacs.7b02714.

[42] E.L. Sesti, E.P. Saliba, N. Alaniva, A.B. Barnes, Electron decoupling with cross polarization and dynamic nuclear polarization below 6 K, J. Magn. Reson. 295 (2018) 1–5. doi:10.1016/j.jmr.2018.07.016.

[43] F.J. Scott, E.P. Saliba, B.J. Albert, N. Alaniva, E.L. Sesti, C. Gao, N.C. Golota, E.J. Choi, A.P. Jagtap, J.J. Wittmann, M. Eckardt, W. Harneit, B. Corzilius, S. Th. Sigurdsson, A.B. Barnes, Frequency-Agile Gyrotron for Electron Decoupling and Pulsed Dynamic Nuclear

Polarization, J. Magn. Reson. 289 (2018) 45–54. doi:10.1016/j.jmr.2018.02.010.

[44] A.E. Bennett, C.M. Rienstra, M. Auger, K. V Lakshmi, R.G. Griffin, Heteronuclear decoupling in rotating solids, J. Chem. Phys. 103 (1995) 6951–6958. doi:10.1063/1.470372.

[45] K.R. Thurber, R. Tycko, Measurement of sample temperatures under magic-angle spinning from the chemical shift and spin-lattice relaxation rate of 79 Br in KBr powder, J. Magn. Reson. 196 (2009) 84–87. doi:10.1016/j.jmr.2008.09.019.

[46] CPI, CGY-8026 Gyrotron Ascillator, (2012) 1–2.

[47] A.B. Barnes, E.A. Nanni, J. Herzfeld, R.G. Griffin, R.J. Temkin, A 250 GHz gyrotron with a 3 GHz tuning bandwidth for dynamic nuclear polarization, J. Magn. Reson. 221 (2012) 147–153. doi:10.1016/j.jmr.2012.03.014.

[48] F.J. Scott, N. Alaniva, N.C. Golota, E.L. Sesti, E.P. Saliba, L.E. Price, B.J. Albert, P. Chen, R.D. O'Connor, A.B. Barnes, A Versatile Custom Cryostat for Dynamic Nuclear Polarization Supports Multiple Cryogenic Magic Angle Spinning Transmission Line Probes, J. Magn. Reson. 297 (2018) 23–32. doi:10.1016/J.JMR.2018.10.002.

[49] F.J. Scott, E.L. Sesti, E.J. Choi, A.J. Laut, J.R. Sirigiri, A.B. Barnes, Magic angle spinning NMR with metallized rotors as cylindrical microwave resonators, Magn. Reson. Chem. 56 (2018) 831–835. doi:10.1002/mrc.4744.

Chapter 4:

Electron Decoupling with Chirped Microwave Pulses for Rapid Signal Acquisition and Electron Saturation

Foreword

This chapter is a reproduction of the Angewandte Chemie publication, "Electron Decoupling with Chirped Microwave Pulses for Rapid Signal Acquisition" (*Alaniva, N.; *Saliba, E.P.; Sesti, E. L.; Barnes, A. B. (2019) "Electron Decoupling with Chirped Microwave Pulses for Rapid Signal Acquisition". Angewandte Chemie. **131** (22): 7337 – 7340. doi: 10.1002/ange.201900139), done so with permission from the journal, Angewandte Chemie. Here, the electron decoupling is used to saturate trityl radical electron spins, and their longitudinal recovery is then observed through nuclear spin signal using short periods of dynamic nuclear polarization (DNP). This "direct DNP" transfer limits the enhanced nuclear signal to those spins that are located closer to the polarizing trityl radical by limiting the amount of time for spin diffusion of the polarization. In the sequences that use a 5 ms DNP period the radiofrequency (RF) duty cycle (ratio of on/off) eclipses 50%, which greatly increases the possibility of breakdown in the RF circuit. With cryogenic sample cooling and the transmission line probe's power-handling capability, this breakdown was avoided.

4.1 Overview

Dynamic nuclear polarization (DNP) increases NMR sensitivity by transferring polarization from electron to nuclear spins. Here we demonstrate that electron decoupling enables improved observation of DNP-enhanced ^{13}C spins in direct dipolar contact with electron spins, thereby leading to an optimal delay between transients largely governed by relatively fast electron relaxation. Signal acquisition constitutes 12% of the total experimental time, significantly increasing signal-to-noise per unit time. We report the first measurement of electron longitudinal relaxation (T_{1e}) during magic-angle spinning (MAS) NMR through observation of DNP-enhanced NMR (T_{1e} = 40 ± 6 ms, 40 mM trityl 4.0 kHz MAS, 4.3 K). With a 5 ms DNP period, electron decoupling results in a 195% increase in signal intensity. Chirped microwave pulses and MAS at 4.3 K are achieved with a custom spectrometer. MAS at 4.3 K, DNP, electron decoupling, and short recycle delays improves the sensitivity of ^{13}C in the vicinity of the polarizing agent. This is the first demonstration of recovery times between MAS-NMR transients being governed by short electron T_1 and fast DNP transfer.

4.2 MAS Background and Introduction to Rapid Signal Acquisition

Magic angle spinning (MAS) nuclear magnetic resonance (NMR) spectroscopy reveals structural and dynamical information on a range of molecular architectures including membrane proteins[1–6], fibrils[7–10], and interfaces[11–14]. Mechanical rotation of the sample about the magic angle of 54.7^o with respect to the magnetic field partially averages anisotropic interactions of the magnetic resonance Hamiltonian, improving spectral resolution and sensitivity[15–18]. Often, sensitivity is also increased through the transfer of polarization from spins with stronger Zeeman

interactions via radiofrequency[16,19] or microwave irradiation. In the case of DNP, hyperfine interactions are required to transfer spin polarization from electron to nuclear spins[20–25].

DNP transfer mechanisms require polarizing agents exhibiting electron paramagnetic resonance (EPR)[26]. Here we use a stable organic mono-radical, trityl (Finland radical), which has a relatively narrow EPR lineshape[27]. The narrow electron spin resonance and high-power microwave chirps generated by a custom-built frequency-agile gyrotron enable time-domain manipulation of electronic and hyperfine interactions[28,29]. We have shown that chirped microwave pulses can partially decouple the electron-nuclear spin interaction after DNP in a method known as electron decoupling, with a more pronounced effect on observed nuclear spins in direct proximity to electron spins[30,31].

DNP experiments typically require seconds to hours to spread enhanced polarization via nuclear spin diffusion to chemical sites of interest[32–34]. This slow spin diffusion significantly limits experiments. DNP is faster if nuclear spins proximal to the electron are polarized directly through hyperfine interactions. However, such direct DNP requires electron decoupling after the polarization transfer period to mitigate the detrimental effects of hyperfine interactions on NMR signatures[31,35].

The optimal repetition time for direct DNP is limited by the electron longitudinal relaxation (T_{1e}) and DNP transfer, and not by nuclear spin diffusion. At low temperatures, the T_{1e} can exceed the length of the direct DNP transfer to strongly hyperfine-coupled nuclear spins. This enables T_{1e} measurement through observation of DNP-enhanced NMR signals. Indirect DNP techniques that rely on spin diffusion cannot be used to measure electron relaxation because the propagation time of enhanced polarization is much longer than T_{1e}. With direct DNP followed by electron decoupling, thousands of transients can be acquired every minute. Here we apply electron

decoupling and a rapid acquisition scheme to observe directly-polarized ^{13}C spins, enabling for the first time measurement of electron longitudinal relaxation in MAS magnetic resonance experiments.

The pulse sequence used to generate electron decoupling is shown in **Figure 4.1**. During the electron decoupling period, the microwave frequency is chirped through the trityl resonance. For control experiments without electron decoupling, the microwaves are chirped off-resonance from trityl or any DNP matching condition to retain similar microwave heating, while not perturbing the spin system. Acquisitions with and without electron decoupling were interwoven sequentially to reduce experimental variability.

Short polarization times of 5 ms and 10 ms were employed to emphasize NMR signals from nuclear spins with strong hyperfine interactions. This results in observation of a small fraction of the total ^{13}C spins present, and worse sensitivity than is commonly achieved with MAS DNP experiments observing all bulk spins. However, transients were collected with minimal delay to improve the sensitivity per unit time (**Figure 4.1**).

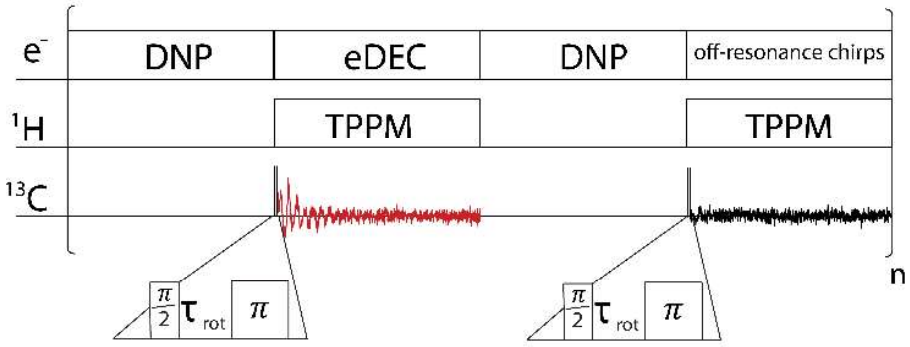

Figure 4.1: *Electron decoupling (eDEC) comparison pulse sequence showing the actual DNP-enhanced signal in the time domain. The DNP period was 5 or 10 ms in these experiments. The horizontal scaling of all time events is accurate for a 5 ms DNP period. τ_{rot} is defined as one rotor period. Two-Pulse Phase-Modulation (TPPM) ^{1}H decoupling is applied at the beginning of the ^{13}C $\pi/2$ pulse[36].*

4.3 Experimental Methods

All experiments performed here were acquired on a sample of 4 M, [U-^{13}C, U-^{15}N, D_7] L-proline (Cambridge Isotopes Laboratories, Tewksbury, MA) and 40 mM trityl (Finland Radical, Oxford Instruments America, Concord, MA) frozen in a glassy matrix composed of 60% d_8-glycerol and 40% D_2O. 36 µL of sample was pipetted into a 3.2 mm outside diameter zirconia rotor. All experiments described were performed with 4.0 kHz of magic angle spinning.

A sample temperature of 4.3 K was established with a liquid helium variable temperature stream, and monitored with a calibrated temperature sensor in all MAS experiments[50]. RF and microwave pulses were controlled with a Tecmag Redstone spectrometer (Tecmag, Houston, TX). Microwave chirped pulses were generated with a custom-built frequency-agile gyrotron outputting 40 W (15 W incident on the sample), resulting in an estimated electron nutation frequency of 0.7 MHz. Microwave power is delivered to the sample through a series of copper mirrors and custom-designed corrugated transmission lines manufactured at Washington University in St. Louis[51].

DNP was performed at the zero-quantum solid effect condition (197.719 GHz). Electron decoupling and electron saturation were performed with linear frequency chirps centered on the trityl resonant frequency of 197.640 GHz. The chirps swept over a range of 103 MHz in 13.75 µs. In experiments without electron decoupling, off-resonance chirps were centered at 197.863 GHz and swept through a range of 48 MHz over 13.75 µs.

All experiments were performed at 7 T (^{1}H – 300.179 MHz; ^{13}C – 75.4937 MHz). NMR experiments utilized Two-Pulse Phase-Modulation (TPPM) ^{1}H decoupling at a nutation frequency of 20 kHz. This low decoupling power was effective due to the high level of

deuteration of the sample. ^{13}C pulses at a nutation frequency of 100 kHz were used in all experiments.

4.4 Electron Decoupling at Short Polarization Times

The spectra in **Figure 4.2a** and **Figure 4.2b** were obtained with polarization times of 10 and 5 ms, respectively. With electron decoupling, the integrated area of the proline carbonyl resonance increases by 87% in the 10 ms polarization case and by 195% in the 5 ms case. These results are dramatic improvements over previously reported intensity gains from electron decoupling[31], emphasizing improvements from electron decoupling achieved while observing directly hyperfine-coupled nuclear spins. The linewidth of the electron decoupling spectrum after 10 ms of DNP is not noticeably affected, while the electron decoupling spectrum taken with 5 ms of DNP actually shows a 17% increase in linewidth. This could be due to spins that were narrowed sufficiently for their signal to be distinguished from the noise, but not enough to decrease the overall linewidth, thus adding broader components to the spectrum. The currently available electron nutation frequency of 0.7 MHz, predicted with 15 W of incident microwave power,[29,31] yields electron spin control only sufficient to decouple weaker hyperfine interactions. Electron decoupling of stronger hyperfine interactions will require a higher electron nutation frequency for fast adiabatic passages and improved broadband spin decoupling.

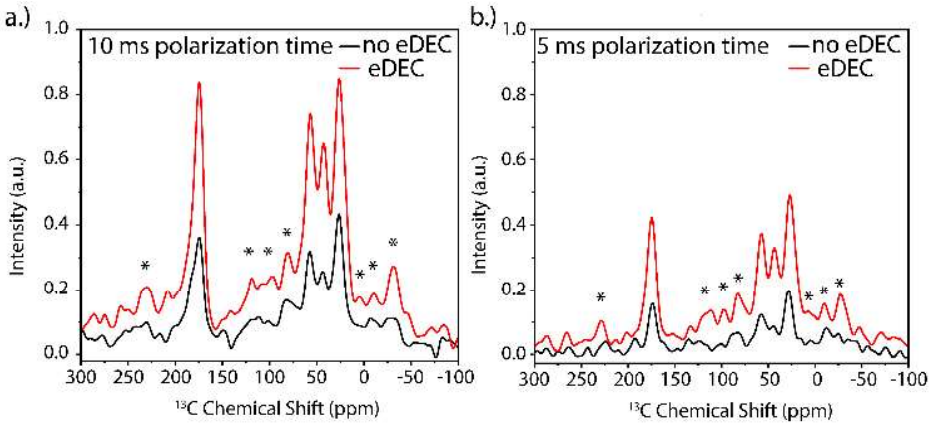

***Figure 4.2**: Comparison of ^{13}C direct spectra taken with (red) and without (black) (57,344 transients each) at **a.)** 10 ms and **b.)** 5 ms of polarization time. Asterisks denote spinning sidebands. In both **a.)** and **b.)** the sample is 36 µL of 4 M, [U-^{13}C, U-^{15}N, D_7] L-proline and 40 mM trityl frozen in a glassy matrix composed of 60% d_8-glycerol and 40% D_2O, and the temperature is 4.3 K.*

Figure 4.3 compares a Hahn echo to a Bloch decay, both with electron decoupling and a DNP period of 10 ms. The Hahn echo significantly improves the baseline. An expansion around the NMR resonances is shown in **Figure 4.3b**. Broad features, which relax on a time scale faster than the echo delay, are filtered out with a Hahn echo. Further improvements to microwave technology will enable electron decoupling of the stronger hyperfine interactions manifested in these broad features.

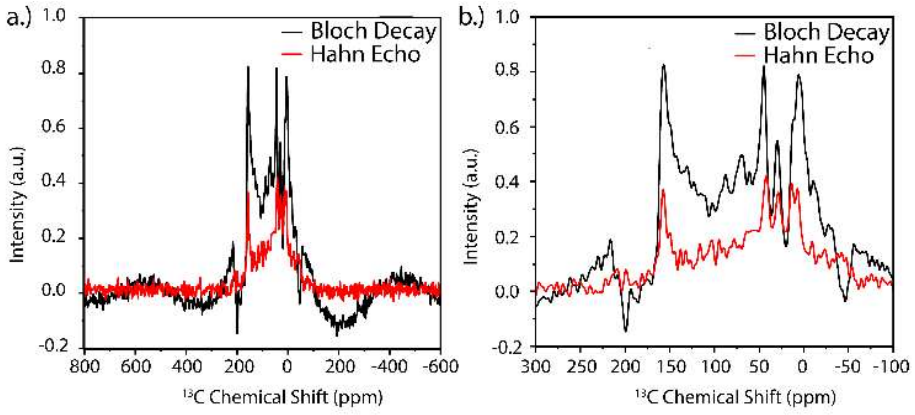

***Figure 4.3**: **a.)** Electron decoupling spectra acquired with a Hahn echo (red) and with a Bloch decay (black). The rolling baseline of the Block decay spectrum is apparent. **b.)** An expansion of the spectra shown in **a.)**. The sample in both experiments is 36 µL of 4 M, [U-^{13}C, U-^{15}N, D_7] L-proline and 40 mM trityl frozen in a glassy matrix composed of 60% d_8-glycerol and 40% D_2O, and the temperature is 4.3 K.*

4.5 Electron Saturation Recovery

The saturation recovery pulse sequence used to measure the T_{1e} of the trityl radical is shown in **Figure 4.4**. The train of chirped microwave pulses applied during free induction decay (FID) for electron decoupling saturates the electron spins. Although the mechanism of electron decoupling is yet to be precisely determined, decoupling electron spins does require coherent manipulation of hyperfine interactions. We note that electronic spin saturation does not remove the microscopic local field seen by each nuclear spin, and is therefore not the mechanism of electron decoupling in the MAS experiments we report here.[29,37]

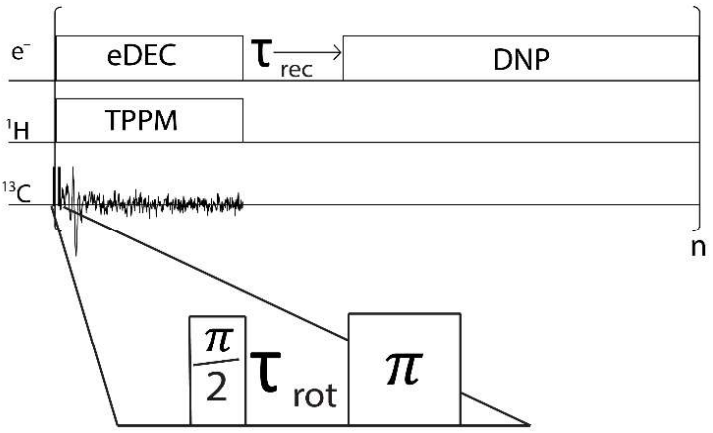

Figure 4.4*: The pulse sequence used for electron saturation recovery. Electron decoupling was applied over 5.376 ms, which includes a 5.12 ms acquisition period; here the DNP period is 10 ms.* τ_{rec} *ranges from 0.005 ms to 128 ms.*

An electron spin recovery period without microwaves was employed directly after NMR signal acquisitions. The microwave output was terminated by quickly changing the potential of the gyrotron anode. The lack of microwave irradiation allowed the electron spins to relax for variable amounts of time to determine T_{1e}.

The total electron magnetization buildup curve, measured using the pulse sequence of **Figure 4.4**, is shown in **Figure 4.5a**. Data points at 0.005 ms, 4 ms, 8 ms, 16 ms, 20 ms, 64 ms, and 128 ms were obtained. Data were fit to the function $M(t) = M_1 + M_0\left(1 - e^{-t/T_{1e}}\right)$.

Shorter recovery periods resulted in smaller magnetization, requiring more transients to achieve sufficient signal-to-noise. Intensities were then scaled with respect to the number of transients. The measured T_{1e} of 40 mM trityl spinning at 4.0 kHz was 40 ± 6 ms. **Figure 4.5b** and **Figure 4.5c** display spectra collected at 4 ms and 128 ms of electron recovery time, respectively. Interestingly, off-resonance frequency chirps seem to also partially saturate the electrons, although not nearly to the degree of on-resonance chirps.

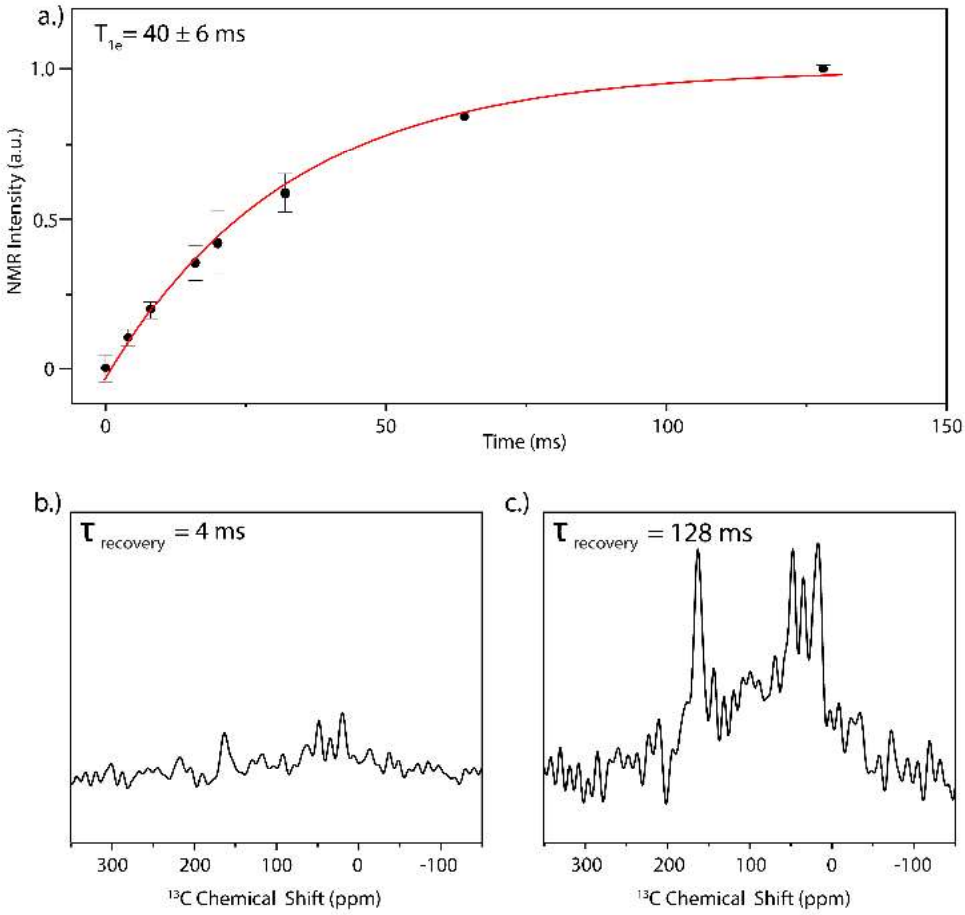

***Figure 4.5**: Electron saturation recovery. **a.)** NMR signal intensity as a function of the electron recovery time fits to a T_{1e} of 40 ± 6 ms. Also shown are spectra with **b.)** 4 ms electron recovery time and **c.)** 128 ms electron recovery time. The sample in these recovery experiments is 36 µL of 4 M, [U-^{13}C, U-^{15}N, D_7] L-proline and 40 mM trityl frozen in a glassy matrix composed of 60% d_8-glycerol and 40% D_2O, and the temperature is 4.3 K.*

Due to the comparable lengths of the DNP period, signal acquisition, and electron longitudinal magnetization recovery, the optimal recovery period is not $1.26 \times T_{1e}$[38,39]. In the experiments described here, the optimal recovery period is $1.69 \times T_{1e}$.

4.6 Conclusion and Outlook

In conclusion, electron decoupling permits better observation of hyperfine coupled nuclear spins by mitigating the electron-nuclear interaction. Hyperfine couplings are used to directly polarize nuclear spins, thereby eliminating the requirement for slow nuclear spin diffusion, and greatly accelerating data acquisition. We show that optimal recycle delays are governed by the relatively fast electron longitudinal relaxation (T_{1e}). This is the first demonstration of the measurement of longitudinal electron relaxation under MAS (T_{1e} = 40 +/- 6 ms).

Techniques, like those presented in this manuscript, will be important in localized DNP experiments in which radicals are attached to targeted small molecules, or present within larger biomolecular achitectures[22,40–44]. Short recovery periods also significantly improve the sensitivity per unit time of MAS NMR, and are expected to play a prominent role in the future of magnetic resonance experiments. The manipulation of electron spins in the time domain, as demonstrated here, is an important step toward implementing pulsed DNP-MAS[29,45–48]. Lastly, further advancements in microwave and spinning technology will better enable sensitive EPR detection with MAS[30,49].

4.7 Acknowledgements

This work received financial support from the National Institute of Health (NIH) in the form of the grant: DP2-GM119131; the National Science Foundation in the form of the grant: NSF-IDBR (CAREER DBI-1553577); and the Camille Dreyfus Teacher-Scholar Awards Program.

We thank Chukun Gao, Faith Scott, Brice Albert, Pin-Hui Chen, and Lauren Price for helpful discussions. We also thank the reviewers of this manuscript for their insight.

References

[1] W. T. Franks, D. H. Zhou, B. J. Wylie, B. G. Money, D. T. Graesser, H. L. Frericks, G. Sahota, C. M. Rienstra, *J. Am. Chem. Soc.* **2005**, *127*, 12291–12305.

[2] Q. Z. Ni, T. V. Can, E. Daviso, M. Belenky, R. G. Griffin, J. Herzfeld, *J. Am. Chem. Soc.* **2018**, *140*, 4085–4091.

[3] A. McDermott, *Annu. Rev. Biophys.* **2009**, *38*, 385–403.

[4] M. T. Eddy, L. Andreas, O. Teijido, Y. Su, L. Clark, S. Y. Noskov, G. Wagner, T. K. Rostovtseva, R. G. Griffin, *Biochemistry* **2015**, *54*, 994–1005.

[5] J. S. Retel, A. J. Nieuwkoop, M. Hiller, V. A. Higman, E. Barbet-Massin, J. Stanek, L. B. Andreas, W. T. Franks, B. J. Van Rossum, K. R. Vinothkumar, et al., *Nat. Commun.* **2017**, *8*, 1–10.

[6] R. Linser, M. Dasari, M. Hiller, V. Higman, U. Fink, J. M. Lopez Del Amo, S. Markovic, L. Handel, B. Kessler, P. Schmieder, et al., *Angew. Chemie - Int. Ed.* **2011**, *50*, 4508–4512.

[7] A. T. Petkova, R. D. Leapman, Z. Guo, **2005**, *307*, 262–265.

[8] C. L. Hoop, H.-K. Lin, K. Kar, G. Magyarfalvi, J. M. Lamley, J. C. Boatz, A. Mandal, J. R. Lewandowski, R. Wetzel, P. C. A. van der Wel, *Proc. Natl. Acad. Sci.* **2016**, *113*, 1546–1551.

[9] A. B. Siemer, C. Ritter, M. Ernst, R. Riek, B. H. Meier, *Angew. Chem. Int. Ed.* **2005**, *44*, 2–5.

[10] T. Theint, P. S. Nadaud, D. Aucoin, J. J. Helmus, S. P. Pondaven, K. Surewicz, W. K. Surewicz, C. P. Jaroniec, *Nat. Commun.* **2017**, *8*, DOI 10.1038/s41467-017-00794-z.

[11] J. R. Long, W. J. Shaw, P. S. Stayton, G. P. Drobny, *Biochemistry* **2001**, *40*, 15451–15455.

[12] S. Cadars, N. Mifsud, A. Lesage, J. D. Epping, N. Hedin, B. F. Chmelka, L. Emsley, *J. Phys. Chem. C* **2008**, *112*, 9145–9154.

[13] M. Bertmer, R. C. Nieuwendaal, A. B. Barnes, S. E. Hayes, *J. Phys. Chem. B* **2006**, *110*, 6270–6273.

[14] O. A. McCrate, X. Zhou, C. Reichhardt, L. Cegelski, *J. Mol. Biol.* **2013**, *425*, 4286–4294.

[15] I. J. Lowe, *Phys. Rev. Lett.* **1959**, *2*, 285–287.

[16] J. Schaefer, E. O. Stejskal, *J. Am. Chem. Soc.* **1976**, *98*, 1031–1032.

[17] E. R. Andrew, *Philos. Trans. R. Soc. A Math. Phys. Eng. Sci.* **1981**, *299*, 505–520.

[18] M. Ernst, **2001**, *348*, 1–10.

[19] A. Pines, M. G. Gibby, J. S. Waugh, **1972**, *56*, 1776.

[20] B. Corzilius, A. A. Smith, A. B. Barnes, C. Luchinat, I. Bertini, R. G. Griffin, *J. Am. Chem. Soc.* **2011**, *133*, 5648–5651.

[21] E. O. Stejskal, J. Schaefer, R. A. McKay, *J. Magn. Reson.* **1977**, *25*, 569–573.

[22] B. J. Wylie, B. G. Dzikovski, S. Pawsey, M. Caporini, M. Rosay, J. H. Freed, A. E. McDermott, *J. Biomol. NMR* **2015**, *61*, 361–367.

[23] Q. Z. Ni, E. Markhasin, T. V. Can, B. Corzilius, K. O. Tan, A. B. Barnes, E. Daviso, Y. Su, J. Herzfeld, R. G. Griffin, *J. Phys. Chem. B* **2017**, *121*, 4997–5006.

[24] G. J. Gerfen, L. R. Becerra, D. A. Hall, R. G. Griffin, R. J. Temkin, D. J. Singel, *J. Chem. Phys.* **1995**, *102*, 9494–9497.

[25] K. Thurber, R. Tycko, *J. Magn. Reson.* **2016**, *264*, 99–106.

[26] A. S. Lilly Thankamony, J. J. Wittmann, M. Kaushik, B. Corzilius, *Prog. Nucl. Magn. Reson. Spectrosc.* **2017**, *102–103*, 120–195.

[27] A. A. Smith, B. Corzilius, A. B. Barnes, T. Maly, R. G. Griffin, *J. Chem. Phys.* **2012**, *136*, DOI 10.1063/1.3670019.

[28] F. J. Scott, E. P. Saliba, B. J. Albert, N. Alaniva, E. L. Sesti, C. Gao, N. C. Golota, E. J. Choi, A. P. Jagtap, J. J. Wittmann, et al., *J. Magn. Reson.* **2018**, *289*, DOI 10.1016/j.jmr.2018.02.010.

[29] D. E. M. Hoff, B. J. Albert, E. P. Saliba, F. J. Scott, E. J. Choi, M. Mardini, A. B. Barnes, *Solid State Nucl. Magn. Reson.* **2015**, *72*, DOI 10.1016/j.ssnmr.2015.10.001.

[30] E. P. Saliba, E. L. Sesti, N. Alaniva, A. B. Barnes, *J. Phys. Chem. Lett.* **2018**, *9*, 5539–5547.

[31] E. P. Saliba, E. L. Sesti, F. J. Scott, B. J. Albert, E. J. Choi, N. Alaniva, C. Gao, A. B. Barnes, *J. Am. Chem. Soc.* **2017**, *139*, 6310–6313.

[32] A. E. Dementyev, D. G. Cory, C. Ramanathan, *Phys. Rev. Lett.* **2008**, *100*, 127601-1-127601–4.

[33] T. Maly, A. F. Miller, R. G. Griffin, *ChemPhysChem* **2010**, *11*, 999–1001.

[34] A. J. Rossini, U. De Lyon, A. Zagdoun, U. De Lyon, M. Lelli, U. De Lyon, A. Lesage, C. Coperet, E. T. H. Zürich, A. J. Rossini, et al., *Acc. Chem. Res.* **2013**, *46*, 1942–51.

[35] L. R. Becerra, G. J. Gerfen, R. J. Temkin, D. J. Singel, R. G. Griffin, *Phys. Rev. Lett.* **1993**, *71*, 3561–3564.

[36] A. E. Bennett, C. M. Rienstra, M. Auger, K. V Lakshmi, R. G. Griffin, **2009**, *6951*, DOI 10.1063/1.470372.

[37] S. K. Jain, T. A. Siaw, A. Equbal, C. B. Wilson, I. Kaminker, S. Han, *J. Phys. Chem. C* **2018**, *122*, 5578–5589.

[38] J. S. Waugh, *J. Mol. Spectrosc.* **1970**, *35*, 298–305.

[39] A. D. Bain, D. W. Hughes, C. K. Anand, V. J. Robertson, *Magn. Reson. Chem.* **2010**, 630–641.

[40] T. Viennet, A. Viegas, A. Kuepper, S. Arens, V. Gelev, O. Petrov, T. N. Grossmann, H. Heise, M. Etzkorn, *Angew. Chemie - Int. Ed.* **2016**, *55*, 10746–10750.

[41] R. A. Munro, A. I. Smirnov, V. Ladizhansky, T. I. Smirnova, M. Donohue, S. Milikisiyants, S. Wang, D. Bolton, M. E. Ward, L. S. Brown, *J. Mol. Biol.* **2017**, *429*, 1903–1920.

[42] B. J. Albert, C. Gao, E. L. Sesti, E. P. Saliba, N. Alaniva, F. J. Scott, S. T. Sigurdsson, A.

B. Barnes, *Biochemistry* **2018**, *57*, 4741–4746.

[43] A. N. Smith, M. A. Caporini, G. E. Fanucci, J. R. Long, *Angew. Chemie - Int. Ed.* **2015**, *54*, 1542–1546.

[44] T. Maly, D. Cui, R. G. Griffin, A. F. Miller, *J. Phys. Chem. B* **2012**, *116*, 7055–7065.

[45] K. O. Tan, C. Yang, R. T. Weber, G. Mathies, R. G. Griffin, *Sci. Adv.* **2019**, *5*, 1–8.

[46] A. Henstra, P. Dirksen, W. T. Wenckebach, *Phys. Lett. A* **1988**, *134*, 134–136.

[47] T. V. Can, R. T. Weber, J. J. Walish, T. M. Swager, R. G. Griffin, *Angew. Chemie Int. Ed.* **2017**, 1–6.

[48] S. K. Jain, G. Mathies, R. G. Griffin, *J. Chem. Phys.* **2017**, *147*, 164201.

[49] D. Hessinger, C. Bauer, M. Hubrich, G. Jeschke, H. Spiess, *J. Magn. Reson.* **2000**, *225*, 217–225.

[50] E. L. Sesti, N. Alaniva, P. W. Rand, E. J. Choi, B. J. Albert, E. P. Saliba, F. J. Scott, A. B. Barnes, *J. Magn. Reson.* **2018**, *286*, 1–9.

[51] F. J. Scott, N. Alaniva, N. C. Golota, E. L. Sesti, E. P. Saliba, L. E. Price, B. J. Albert, P. Chen, R. D. O'Connor, A. B. Barnes, *J. Magn. Reson.* **2018**, *297*, 23–32.

Chapter 5:

Electron Decoupling with ^{14}N-Endofullerene at 90 K

Foreword

This chapter features data that is, as of the submission of this dissertation, unpublished. Here, the frequency-agile gyrotron is used to map out the solid effect ^{13}C-enhancement profile and perform electron decoupling using ^{14}N-endofullerene. The sample is a polycrystalline powder comprised C_{60} (natural abundance ^{13}C) fullerene and $^{14}N@C_{60}$ (atomic ^{14}N, with electron spin-3/2, trapped within the C_{60} cage) present at a concentration of 160 parts-per-million (ppm). The DNP enhancement profile follows the three-peak pattern of the ^{14}N electron spin-3/2 electron paramagnetic resonance profile, whose splitting is a result of the coupling to the quadrupolar ^{14}N nucleus. Through combination of the vacuum-jacketed cryogen delivery system with the radiofrequency probe and the frequency-agile gyrotron, ^{13}C DNP experiments with electron decoupling are performed at 90 K. At this temperature the rotational motion of the C_{60} molecules is arrested and the broadening effects of anisotropic chemical shift and dipolar interactions can be observed. Here, electron decoupling is used to detect the apparent anisotropy of the electron-nuclear dipolar interaction.

5.1 Overview

Electron decoupling is a technique that uses frequency-chirped microwaves to attenuate the electron-nuclear dipolar interaction. This increases intensity and improves the resolution of the observed dynamic nuclear polarization (DNP)-enhanced NMR signal. Here electron decoupling

is performed on a powder sample of natural abundance C_{60} with ^{14}N-endofullerene ($^{14}N@C_{60}$) present at 160 ppm, at 90 K while magic-angle spinning (MAS) at 4.0 kHz. With 7 s of DNP, electron decoupling affords a 10% increase in intensity in the center band signal. Interestingly, a difference in the amount of recovered signal intensity is observed at different spinning sidebands and the center band, especially with a polarization time of 7 s. This difference can be attributed to the small but noticeable hyperfine anisotropy between the unpaired electron in the $^{14}N@C_{60}$ and the ^{13}C spins in the network of surrounding C_{60} molecules, and the lack of motion in the fullerene crystal structure at 90 K.

5.2 C_{60} and $^{14}N@C_{60}$: Introduction

Buckminsterfullerene (here, referred to by its chemical formula C_{60} as well as the more general term, fullerene) is an allotrope of carbon comprised of 60 carbon atoms that are assembled in a truncated icosahedron, with 12 pentagonal faces and 20 hexagonal faces [1]. Above ~260 K these molecules assemble into a face-centered-cubic phase, and rapid molecular reorientation averages out the anisotropy present from the chemical shift of the ^{13}C spins [2]. Below 260 K molecular motion becomes ordered about a single direction and at 90 K, rotational molecular motion is nearly completely halted. Below 90 K, adjacent C_{60} molecules within a crystallite face one another so that the electron-rich bonds that comprise the pentagon shapes overlap with the electron-poor pentagon centers [2, 3]. This loss of molecular motion reveals a chemical shift anisotropy of the C_{60} sample, which can be observed with MAS NMR through the varied intensity of spinning sidebands [4, 5].

$^{14}N@C_{60}$ is a compound that contains a single atomic nitrogen within the C_{60} cage is not chemically bonded to any of the carbon atoms of that cage. There are a few different ways to generate this product, but all methods follow the general scheme of nitrogen bombardment on a

growing film of fullerene. It has been estimated that the nitrogen must overcome an energy barrier of ~20 eV to penetrate the fullerene. Due to the nature of this process, low concentration of the $^{14}N@C_{60}$ is present (~160 parts per million (ppm)) after bombardment [6].

The fullerene within which the nitrogen is trapped provides an extremely isotropic environment for the 3/2 electron spin on the atomic nitrogen[7]. Electron Paramagnetic Resonance (EPR) and dynamic nuclear polarization (DNP) have been performed on this compound, as the unpaired electron that occupies the p-orbitals makes for a paramagnetic species. EPR experiments, such as Electron-Nuclear Double Resonance have been performed that reveal an anisotropic component of the hyperfine interaction between the ^{13}C spins (on both local C_{60} and long-range C_{60}) and the unpaired electron of the trapped nitrogen [8].

The isotropic, non-engaging, concave interior of the fullerene molecule results in relatively long electron-spin relaxation times for $^{14}N@C_{60}$. This, combined with the ability of fullerene molecules to be placed on Si surfaces make it an exciting compound for devices, such as an electron-spin quantum computer system [9].

5.3 Dynamic Nuclear Polarization with $^{14}N@C_{60}$

The mechanism for DNP with $^{14}N@C_{60}$ is the solid effect. The sparsity of the ^{14}N-trapped species and, more importantly, the narrow width of the EPR lineshape basically remove the consideration of cross effect and especially thermal mixing as potential mechanisms. The enhancement profile for the positive solid effect condition ^{13}C-enhancment is obtained by varying the microwave output frequency on the frequency agile gyrotron for separate experiments, using a polarization time of 30 s and combining four transients to achieve sufficient signal-to-noise for accurate measurements.

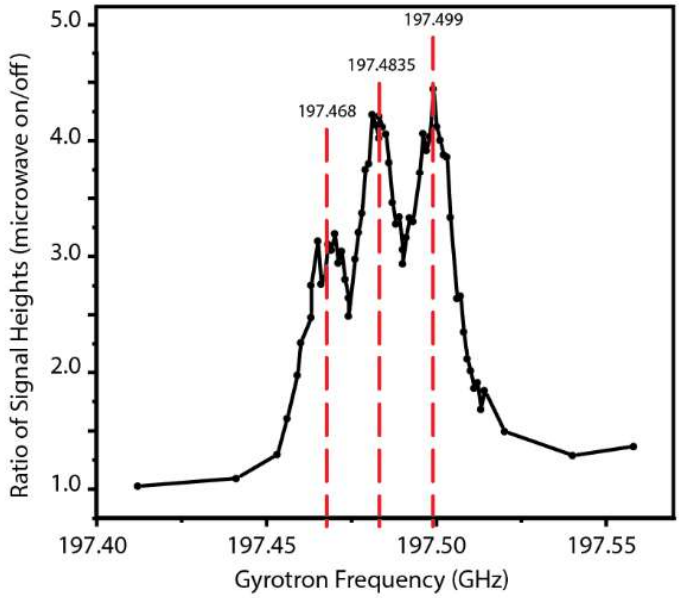

***Figure 5.1**: Double-quantum solid effect ^{13}C-enhancement profile for $N@C_{60}$, using 30 s for DNP period. Sample is C_{60} with 160 ppm $^{14}N@C_{60}$, spinning at 4.0 kHz at the magic angle at a temperature of 90 K.*

Shown below is the enhancement profile for the double-quantum solid effect (positive ^{13}C enhancement). Each point represents a different DNP experiment with the microwave frequency being altered for each experiment by varying the anode potential on the frequency-agile gyrotron. The ~15 MHz splitting is consistent with the interaction of the electron spin-3/2 with the spin-1 ^{14}N nuclear spin. The three peaks correspond to three separate "matching conditions" for the double-quantum solid effect, and their approximate frequencies are called out with the red dashed lines. Microwave irradiation for DNP was set at 197.483 GHz. Electron decoupling experiments were performed with the microwave frequency modulations centered on 197.558 GHz.

5.4 Electron Decoupling at 90 K

Since there are no protons present in the sample, the ^{13}C DNP positive enhancement condition of 197.483 GHz was used, and proton decoupling was not applied during the acquisition time of the experiment. A Bloch decay (^{13}C 90-degree pulse followed by acquisition) was used, with 8 transients summed for 30 s experiments and 16 transients for 7 s experiments. Electron decoupling was applied immediately after DNP periods of 30 s and 7 s. The comparison between spectra with and without electron decoupling for the 30 s and 7 s cases are shown in **Figure 5.2** and **Figure 5.3**, respectively. In these figures, the spectra are focused on the main NMR

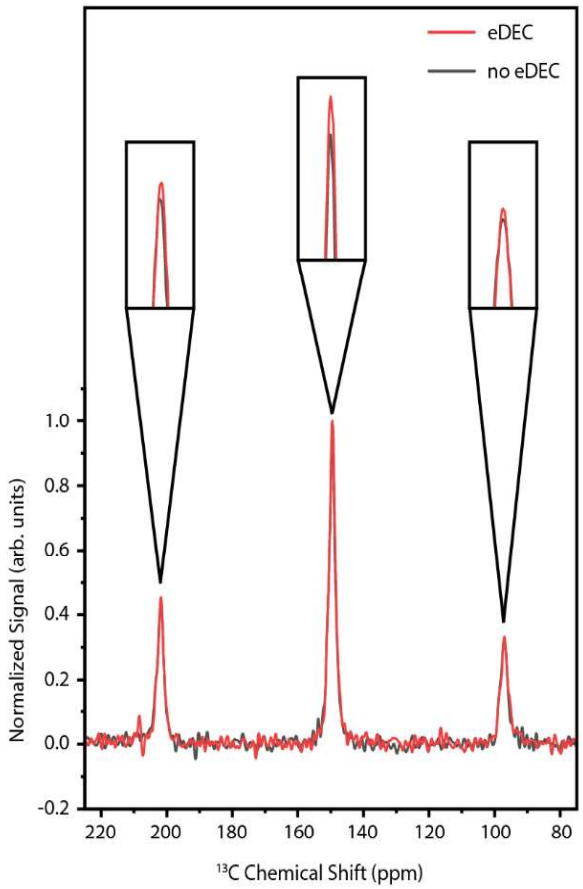

***Figure 5.2**: Compared spectra, with and without electron decoupling; 30 s DNP period. Sample is C_{60} with 160 ppm $^{14}N@C_{60}$, spinning at 4.0 kHz at the magic angle at a temperature of 90 K.*

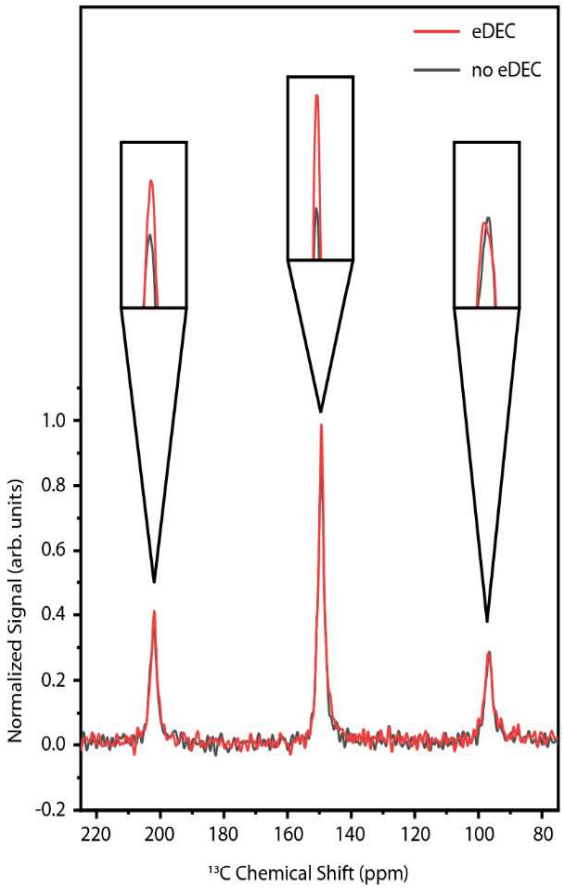

***Figure 5.3**: Compared spectra, with and without electron decoupling; 7 s DNP period. Sample is C_{60} with 160 ppm $^{14}N@C_{60}$, spinning at 4.0 kHz at the magic angle at a temperature of 90 K.*

signature and the first-order spinning sidebands. The intensity of the spinning sideband corresponds to the envelope of the broad lineshape that results from ^{13}C anisotropic interactions with other nuclear spins and electron spins.

With electron decoupling, the gain in signal intensity of the center peak with a DNP period of 30 s is ~3%, while the gain in signal intensity of the center peak with 7 s of DNP is ~10%. In the case of 30 s DNP, electron decoupling brings improvements of < 3% in signal intensity on the spinning sidebands (the first order sidebands are also called out in **Figure 5.2**). With 7 s DNP, the effect of electron decoupling is different across the center signature and each of the spinning sidebands. The center peak experiences an increase in signal intensity of 10%; the spinning sideband at 202 ppm also increases by ~10%; but the spinning sideband at 96 ppm experiences negligible increase in intensity with electron decoupling (**Figure 5.3**). These spectra were fit and areas obtained using the program, Dmfit [10].

5.5 Discussion

The presence of differences in recovered intensity across the lineshape for C_{60} fullerene at 90 K can be explained by the structure and dynamics (or lack thereof) of the sample at 90 K and the presence of an anisotropic hyperfine-dipolar interaction between the paramagnetic $^{14}N@C_{60}$ centers and both local and long-range ^{13}C nuclei. This anisotropic interaction and the spin diffusion/DNP buildup within the sample can explain the discrepancy in the electron decoupling effect between the 7 s and 30 s polarization experiments. The anisotropy of the electron-nuclear dipolar interaction has been documented with EPR techniques [8], but here we propose that it can be observed through DNP-enhanced NMR signal with the use of electron decoupling.

Above 90 K there is some rotational motion of the fullerene cage, as it switches between energetically favorable orientations within the crystallite. Above 260 K, there is enough rotation that the broadening due to anisotropic interactions, like chemical shift anisotropy, are completely averaged and a single, narrow ^{13}C NMR signature is observed. At 90 K, this motion is limited enough that the fullerenes mostly remain in their most energetically favorable orientation [2]. Below 260 K, the lack of motion reveals the chemical shift anisotropy in pure C_{60} samples. In the sample studied here, containing 160 ppm $^{14}N@C_{60}$, the interaction of the electron spin-3/2 on the trapped ^{14}N interacts with the ^{13}C spins present on the C_{60} molecules (1.2 ^{13}C nuclei for every two C_{60} molecules). Whereas only NMR techniques are required to reveal the chemical shift anisotropy, a combination of DNP and electron decoupling reveals the effect of that electron-nuclear anisotropic interaction.

Performing DNP prioritizes those spins that interact with the $^{14}N@C_{60}$, as the solid effect mechanism utilizes the electron-nuclear dipolar interaction in the polarization process. And then electron decoupling mitigates that same interaction by disturbing the electron spin state, manipulating the electron spins so that the interaction is partially averaged. Since the sample is spinning and the microwaves are assumed to affect all electron spins in the $^{14}N@C_{60}$s similarly, the differential effect across the NMR lineshape (center peak and spinning sidebands) is attributed to the anisotropy of the electron-nuclear interaction within the crystallite. This can be observed at 90 K because of the lack of motion of the ^{13}C molecules, which prevents averaging of the electron-nuclear dipolar anisotropy.

The difference in the electron decoupling effect *between 7 s and 30 s* DNP can be explained by the diffusion of polarization. It has been shown for a ^{13}C-natural abundance, 170 ppm $^{14}N@C_{60}$ that the DNP buildup time ($T_{1\ DNP}$) at 100 K and 4.0 kHz MAS is 31 s [11]. This means that a

DNP period of 31s will give approximately 63% of the maximum signal that can be attained with DNP NMR. The process of diffusing polarization in a dilute $^{14}N@C_{60}$ sample is still being investigated, but it has been proposed that the spread of polarization during DNP involves an electron-driven spin diffusion mechanism [11]. This mechanism includes the effect of electron-nuclear hyperfine interactions, and doesn't rely solely on electron-nuclear followed by nuclear-nuclear dipolar interactions for the spread of polarization throughout the sample.

A polarization period of 30 s distributes the DNP enhancement to more ^{13}C spins, farther away from the $^{14}N@C_{60}$ polarization source than its 7 s counterpart. Thus, at 7 s polarization the number of spins and their location, relative to the $^{14}N@C_{60}$, is different; the DNP-enhanced ^{13}C spins will be located closer to their respective electron spin-3/2 than those in the 30 s experiment. Thus, the difference in the effect of electron decoupling between the two types of experiments can be attributed to a difference in the electron-nuclear dipolar anisotropy among the enhanced ^{13}C spins.

5.6 Conclusion and Outlook

The ability of electron decoupling to mitigate the hyperfine interaction between polarizing electron spins used in DNP and observed nuclear spins has been used to regain signal intensity and resolution [12]. Electron decoupling has also been combined with direct DNP and rapid acquisition to observe the relaxation of the polarizing electron spins [13]. The preliminary results here extend the applicability of electron decoupling to the description of structure and electron nuclear interaction in a sample of C_{60} fullerene with 160 ppm $^{14}N@C_{60}$. Here, a frequency-agile gyrotron is used with cryogenic MAS technology to perform DNP and electron decoupling using $^{14}N@C_{60}$ while spinning at a rate of 4.0 kHz and a temperature of 90 K. At this temperature electron decoupling regains signal intensity, but the degree of this recovered intensity varies

across the NMR lineshape and for different lengths of DNP period. These differences are attributed to the anisotropy in the electron-nuclear dipolar interaction and the location of the DNP-enhanced ^{13}C spins relative to the $^{14}N@C_{60}$.

The next steps involve both simulation and NMR experimentation. Performing simulations and DNP NMR experiments with and without electron decoupling at slower spinning frequencies will provide a more detailed picture of the lineshape effects due to the combined chemical shift anisotropy and hyperfine/dipolar anisotropy. Conducting electron decoupling experiments at shorter DNP periods and at different and higher microwave powers will provide more information about nuclear spins that are located closer/more strongly coupled to the $^{14}N@C_{60}$ electron spin.

A description of the electron-nuclear interaction and the polarization process with $^{14}N@C_{60}$ holds importance samples beyond those containing pure fullerene molecules. The long electron relaxation properties at 90 K and below make paramagnetic endofullerenes exciting subjects for DNP experiments. Endofullerene DNP agents also demonstrate potential for electron-spin quantum computing and are also a potential localized polarizing agent for biological systems.

5.5 Acknowledgements

We wish to thank Dr. Bjorn Corzilius for providing the powder sample of 160 ppm $^{14}N@C_{60}$ used in these experiments. Funding for this project was provided by the NSF-IDBR (CAREER DBI-1553577), the NIH Director's New Innovator Award from the National Institutes of Health (DP2GM119131), and a Camille Dreyfus Teacher-Scholar Award.

References

[1] Kroto, H. W.; Heath, J. R.; O'Brien, S. C.; Curl, R. F.; Smalley, R. E. (1985). "C_{60}: Buckminsterfullerene". Nature. **318** (6042): 162–163

[2] David, W. I. F.; Ibberson, R. M.; Matthewman, J. C.; Prassides, K.; Dennis, T. J. S.; Hare, J. P.; Kroto, H. W.; Taylor, R.; Walton, D. R. M. (1991). "Crystal structure and bonding of ordered C_{60}". Nature. **353:** 147—149

[3] David, W. I. F.; Ibberson, R. M.; Dennis, T. J. S.; Hare, J. P.; Prassides, K. (1992) "Structural Phase Transitions in the Fullerene C_{60}". Europhys. Lett. **18** (3): 219—225

[4] Tycko, R.; Dabbagh, G.; Fleming R. M.; Haddon R. C.; Makhija A. V.; Zahurak, S. M. (1991) "Molecular Dynamics and the Phase Transition in Solid C_{60}". Phys. Rev, Lett. **67** (14): 1886—1889

[5] Johnson, R. D.; Bethune D. S.; Yannoni C. S. (1992) "Fullerene Structure and Dynamics: A Magnetic Resonance Potpourri". Acc. Chem. Res. **25**: 169—175

[6] Pietzak, B.; Weidinger, A.; Dinse, K.-P.; Hirsch, A. (2002) "Group V endohedral fullerenes: N@C_{60}, N@C_{70}, P@C_{60}". Endofullerenes: A New Family of Carbon Clusters. **Ch. 2**: 13—65

[7] Wittmann, J. J.; Can, T. V.; Eckardt, M.; Harneit, W.; Griffin, R. G.; Corzilius, B. (2018) "High-precision measurement of the electron spin g factor of trapped atomic nitrogen in the endohedral fullerene N@C_{60}". J. of Mag. Res. **290**: 12—17

[8] Weiden, N.; Kaess, H.; Dinse, K. -P. (1999) "Pulse Electron Parramagnetic Resonance (EPR) and Electron-Nuclear Double Resonance (ENDOR) Investigation of N@C_{60} in Polycrystalline C_{60}". J. Phys. Chem. **103**: 9826—9830

[9] Harneit, W. (2002) “Fullerene-based electron-spin quantum computer”. Physical Review A - Atomic, Molecular, and Optical Physics. **65** (3A): 1—6

[10] D.Massiot, F.Fayon, M.Capron, I.King, S.Le Calvé, B.Alonso, J.O.Durand, B.Bujoli, Z.Gan, G.Hoatson. (2002) 'Modelling one and two-dimensional solid-state NMR spectra.', Magn. Reson. Chem. **40** 70-76 doi:10.1002/mrc.984

[11] Wittman, J. J.; Eckardt, M.; Harneit, W.; Corzilius, B. (2018) “Electron-driven spin diffusion supports crossing the diffusion barrier in MAS DNP”. PCCP. **20** (16): 11418—11429

[12] E. P. Saliba, E. L. Sesti, F. J. Scott, B. J. Albert, E. J. Choi, N. Alaniva, C. Gao, A. B. Barnes, *J. Am. Chem. Soc.* **2017**, *139*, 6310–6313.

[13] Alaniva, N.; Saliba, E.P.; Sesti, E. L.; Barnes, A. B. (2019) ““Electron Decoupling with Chirped Microwave Pulses for Rapid Signal Acquisition”. Angewandte Chemie. **131** (22): 7337 – 7340. doi: 10.1002/ange.201900139

Chapter 6: Conclusions and Outlook

6.1 Summary

This dissertation presents several developments in instrumentation that make cryogenic magic-angle spinning (MAS) dynamic nuclear polarization (DNP) experiments possible. These include transmission-line radiofrequency nuclear magnetic resonance (NMR) probes, a high-power frequency-agile gyrotron, and a transfer line system for efficient cryogen delivery and insulation. The transmission-line NMR probe is customized to support MAS from 90 K down to 4.2 K. Microwave and vacuum-jacketed cryogen-transfer couple to the top of the probehead, allowing for adequate customized insulation to be installed on the NMR probe itself.

Improvements to the design of the frequency-agile gyrotron result in over 100 W of microwave power output, which is then used for the demonstration of frequency-chirped DNP. The frequency agility of these custom gyrotrons are used to decouple the dipolar hyperfine interaction between the paramagnetic polarizing agents and the observed nuclei. Electron decoupling is paired with the high-power capability of the transmission-line probes to perform direct DNP, rapid signal acquisition experiments to observe the effect of electron decoupling on nuclei close to their polarizing sources. This is then taken a step further to encode the longitudinal recovery of the electron spins within the enhanced nuclear signal and define the electron longitudinal relaxation through DNP NMR MAS.

Electron decoupling is then applied to a novel system ($^{14}N@C_{60}$) to observe differences in the electron-^{13}C dipolar interaction within the polycrystalline fullerene sample. This demonstrates an ability to observe structural details involving electrons and nuclear spins through DNP-enhanced NMR signal in a MAS sample. Further work involving simulation of the electron-nuclear

anisotropic interaction with electron decoupling and a more detailed search through the DNP MAS parameter space will provide a clearer picture regarding the electron decoupling process with a paramagnetic species trapped in a C_{60} fullerene.

6.2 Outlook

A next step is described for the experiments involving DNP and electron decoupling with $^{14}N@C_{60}$, which involves further description of that system of dilute polarizing electron spins and the nature of their interactions with the ^{13}C spins. However, the demonstration of both DNP and electron spin control with a frequency-agile gyrotron on this (relatively) isolated electron spin that is protected by the C_{60} cage presents the possibility of installing a fullerene-encaged, protected polarizing agent to different environments for different purposes. Series of precisely-spaced $^{31}P@C_{60}$ have been proposed, in addition to $^{14}N@C_{60}$ and $^{15}N@C_{60}$, as a potential quantum computing system because of the long electron relaxation properties [1]. The ability to control the electron spin with a frequency-agile gyrotron and observe the effect through the electron-nuclear dipolar interaction brings into the realm of possibility quantum computational investigation with DNP NMR.

The protected environment afforded by the C_{60} fullerene presents the possibility of placing the endofullerene polarizing agent in more challenging environments, such as on or potentially in the plasma membrane of a cell. This localization of the DNP polarizing agent, coupled with a better understanding of the diffusion of polarization and electron-nuclear interactions, could lead to exciting, novel in-cell DNP NMR experiments. These localized DNP experiments featuring control of the electron spin could provide better insight into membrane protein insertion-depth, dynamics, and structure.

References

[1] Harneit, W. (2002) “Fullerene-based electron-spin quantum co